Hydrodynamic Modeling for Autonomous Underwater Vehicles Using Computational and Semi-Empirical Methods

By: Jesse Stuart Geisbert

Thesis submitted to the Faculty of the

Virginia Polytechnic Institute and State University

in partial fulfillment of the requirements for the degree of

Master of Science

in

Ocean Engineering

Dr. Craig Woolsey, Committee Chair

Dr. Leigh McCue, Committee Member

Dr. Wayne Neu, Committee Member

May 10th, 2007

Blacksburg, Virginia

Keywords:Math Modeling, AUV, Autonomous Underwater Vehicle, CFD, USAERO

Copyright 2007, Jesse Stuart Geisbert

Hydrodynamic Modeling for Autonomous Underwater Vehicles Using Computational and Semi-Empirical Methods

Jesse Stuart Geisbert

Abstract

Buoyancy driven underwater gliders, which locomote by modulating their buoyancy and their attitude with moving mass actuators and inflatable bladders, are proving their worth as efficient long-distance, long-duration ocean sampling platforms. Gliders have the capability to travel thousands of kilometers without a need to stop or recharge. There is a need for the development of methods for hydrodynamic modeling. This thesis aims to determine the hydrodynamic parameters for the governing equations of motion for three autonomous underwater vehicles. This approach is two fold, using data obtained from computational flight tests and using a semi-empirical approach. The three vehicles which this thesis focuses on are two gliders (*Slocum* and *XRay/Liberdade*), and a third vehicle, the Virginia Tech Miniature autonomous underwater vehicle.

Acknowledgements

There are many people whom I would like to thank for helping me over the past two years in my research and studies that have made this thesis possible. These people have helped me in the classroom, in the office, in the lab, and in all of the general day to day tasks that have occupied my time.

First, I would like to thank my committee for supporting me in this research. I have been able to go to any of them with questions and get direct answers to and help on any of the problems I was having. I further was able to get to know them both inside and outside the classroom, which has made for a much better working atmosphere and experience on my end. Whether it was a BBQ, ice-cream social, or just a friendly meeting, I was always made to feel comfortable and welcomed and I enjoyed each and every interaction I had with you. Thank you.

I would especially like to thank Dr. Craig Woolsey for all the time and energy he has put into this research. Without his almost daily guidance and support I would have found it very easy to give up a long time ago. When I work with Craig, I feel like there is always something new to learn and improve upon, which is an exciting way to approach research. I have been able to count on him for questions and guidance in almost every aspect of my research. It is unexplainably nice to know that if you have a problem and need to contact your advisor, you will get an almost immediate response with a solution that makes sense.

Further, I would like to thank those whom I worked with in the lab on various projects and questions pertaining to this research. Not only did these people answer any trivial questions I had, but they were able to take it a step beyond and show me the implications and importance of what I needed to know. I have been able to know these people too both inside and outside the lab, which has made it very easy and welcoming to come to work every day and see greeting faces. I would especially like to thank Nina Mahmoudian for her help with the viscous parameters on the *Slocum* glider. Nina was able to work with me on several

occasions to gather the proper terms using the proper methods. With her understanding of how and where the values are needed allowed me to better understand why we were doing the research in the first place. To everyone, thank you.

Burke Murray at NSWC-Carderock Division is another person whom I am in debt to for always answering the almost-daily emails and for the occasional meetings we've had over the duration of this research. Without his help and extensive knowledge of USAERO, and the ability to relate and teach the information to me, I would have never been able to use the CFD program and obtain the results I now have. There was never more than a days wait for a response to any email filled with tedious questions that I had sent him. Not only were the responses useful and relevant, but often contained examples of his own work I could look at and manipulate for my own further understanding. Without all of the teaching, files, explanations, and support, I would have never made it this far. Thank you, Burke.

Finally, I would like to thank my fiance and best friend, Jessica Jacobson. I would not be here if not for her and would have pursued other life options long ago if it had not been for her support and friendship and love. She has been the other half of my mental backbone for the past two years. Whenever I was frustrated, upset, or about to give up, she was always there, always positive, and always supportive and understanding to my needs and feelings. She has driven me to excel and helped show me how important it is to be and do all I can while given the time I have here. With her, I can do anything, and a simple thank you will never suffice.

In a final note, I would like to dedicate this thesis and research to the 32 innocent lives that were lost here at Virginia Tech this year on April 16th, 2007. The students who needlessly suffered in this tragic event will live in my memory forever, and to them, who can never finish their goals, dreams, education, ambitions, research, and life, I dedicate my thesis to you.

Contents

1 Introduction **1**

1.1 Buoyancy Driven Underwater Gliders 1

1.2 Standard Modeling Methods 4

1.3 Proposed Approach 6

2 Mathematical Modeling **7**

2.1 Reference Frames 7

2.2 Kinematics 8

2.3 Dynamics 11

2.4 Math Modeling Summary 17

3 Inviscid Coefficients from Computational Flight Tests **18**

3.1 Motivation 18

3.2 USAERO to Compute Inviscid Parameters 20

3.2.1 USAERO Calculation Discussion 22

3.3 Grid Generation and Panel Study 25

3.3.1 Surface Generation 26

3.3.2 Panel Study 26

3.4 Validation of the Approach 36

3.4.1 Sphere 36

3.4.2 Spheroid 38

3.5 Gliders 40

3.5.1 *Slocum* 41

3.5.2 *XRay/Liberdade* 43

3.5.3 Error in Glider Results 45

4 Viscous Coefficients from Semi-empirical Estimates 51

5 Hydrodynamic Modeling for the 475 VTMAUV 55

6 Summary and Conclusions 65

6.1 Future Work and Recommendations 65

A Details of Semi-Empirical Calculations 66

A.1 General Calculations 66

A.2 Repeated Coefficients Calculations 67

A.3 Viscous Coefficients Calculations 69

B *Slocum* Study Results 80

B.1 *Slocum* Panel Study 80

C *XRay/Liberdade* Study Results 83

C.1 *XRay/Liberdade* Panel Study 83

List of Figures

1 Exaggerated Buoyancy Engine Concept 2

2 Reference Frames 7

3 Direction Cosines - Projection of $\boldsymbol{b_1}$ onto $\{\boldsymbol{i}\}$ 8

4 Forces and moments due to constant accelerations in the x-direction 19

5 Constant Force Coefficient in x-direction due to acceleration in x-direction for 5 ft Radius Sphere 21

6 Computing $X_{\dot{u}}$ for a sphere with a 5 ft radius. 22

7 *Slocum* glider in the grid generating program, Surfgen 27

8 Panel Progression 29

9 Pressure Coefficient Error with respect to No. Panels 29

10 Added Mass Error with respect to No. Panels 31

11 475 VTMAUV in Rhinoceros 3.0 31

12 VTMAUV Panel Study 34

13 Final Panel Result for VTMAUV Study 35

14 Sphere with radius r 36

15 Ellipsoid with semi-axes a, b, and c [6] 38

16 *Slocum* glider in Rhinoceros 3.0 41

17 *Slocum* glider in USAERO 42

18 Slocum Added Mass/Inertia due to Linear Accelerations 46

19 Slocum Added Mass/Inertia due to Angular Accelerations 47

20 *XRay* Glider in USAERO/OMNI3D 48

21 *XRay/Liberdade* Linear Acceleration Terms 49

22 *XRay/Liberdade* Angular Acceleration Terms 50

23 475 Glider in USAERO/OMNI3D 55

24 475 Forward Mast Linear Acceleration Terms 59

25 475 Forward Mast Angular Acceleration Terms 60

26 475 Middle Mast Linear Acceleration Terms 61

27 475 Middle Mast Angular Acceleration Terms 62

28 475 Aft Mast Linear Acceleration Terms 63

29 475 Aft Mast Angular Acceleration Terms 64

30 *Slocum* Panel Study 82

31 *XRay/Liberdade* Panel Study 85

List of Tables

1 SNAME notation for for marine vessels; see [6]. 8

2 Coefficient of Pressure Distribution Based on Panels 28

3 Added Mass Comparison for Panel Study of a sphere 30

4 Number of Panels Defined per Study 32

5 Pressure Coefficient Distribution over Panels based on Case No. 33

6 Final Panel Study Distribution 35

7 List of Knowns for Calculations 53

8 Viscous Coefficients for *Slocum* 54

9 Panel Distribution Over *Slocum* Body 80

10 Panel Distribution Over *Slocum* Body 81

11 Final Panel Distribution for *Slocum* 81

12 Panel Distribution Over *XRay/Liberdade* Body 83

13 Pressure Distribution Over *XRay/Liberdade* Body per Study 84

14 Final Panel Distribution on the *XRay/Liberdade* Body 84

Nomenclature/Notation

Variable	Description
$\hat{\cdot}$	cross product equivalent matrix $\hat{\boldsymbol{a}}\boldsymbol{b} = \boldsymbol{a} \times \boldsymbol{b}$
$\bar{\cdot}$	nondimensional value
$\mathbf{0}$	zero vector
$\boldsymbol{b}_i$	basis vector for body frame, i $\in \{1, 2, 3\}$
$\boldsymbol{C}_{\mathrm{f}}$	hydrodynamic coupling matrix
$\boldsymbol{C}_{\mathrm{rb}}$	rigid body coupling matrix
$\mathcal{D}$	drag force
$\boldsymbol{D}_{\omega}$	angular rate damping matrix
$\boldsymbol{F}_{\mathrm{viscous}}$	hydrodynamic force, $[X,\ Y,\ Z]^T$
g	acceleration due to gravity
$\boldsymbol{h}$	angular momentum about body origin
$\boldsymbol{i}_i$	basis vector for inertial frame, i $\in \{1, 2, 3\}$
$\boldsymbol{I}_{\mathrm{rb}}$	rigid body inertia
$\boldsymbol{I}_{\mathrm{f}}$	added inertia
$\boldsymbol{I}_{\mathrm{mm}}$	mass particle inertia about body origin
l	reference length
$\mathcal{L}$	lift force
m	mass of displaced fluid *less* particle m_{p}
m_{rb}	mass of rigid body
m_{v}	total vehicle mass

Variable	Description
m_{p}	lateral mass particle
$\tilde{m}$	excess mass, $m_{\mathrm{v}} - m$
$\boldsymbol{M}_{\mathrm{f}}$	added mass matrix
$\boldsymbol{M}_{\mathrm{rb}}$	vehicle mass matrix
$\boldsymbol{M}_{\mathrm{viscous}}$	hydrodynamic moment, $[L,\ M,\ N]^T$
$\boldsymbol{p}$	inertial linear momentum in body frame
$\boldsymbol{r}_{\mathrm{p}}$	position of lateral mass particle, $\boldsymbol{r}_{\mathrm{p}} = r_{\mathrm{p}}\boldsymbol{b}_2$
$\boldsymbol{r}_{\mathrm{rb}}$	body center of mass (less contribution due to m_{p})
$\boldsymbol{R}$	body to inertial rotation
ρ	density (seawater)
$\mathcal{S}$	side force
$\boldsymbol{T}$	kinetic energy

In addition to the nomenclature described above, we adopt a somewhat standard notation for the dimensional and non-dimensional hydrodynamic parameters commonly referred to as "stability derivatives." These parameters can be divided into inviscid (potential flow) terms and viscous terms. For an underwater vehicle, the primary inviscid hydrodynamic parameters are the components of the generalized added inertia matrix. Following SNAME notation [6], the generalized added inertia matrix is

$$\boldsymbol{M_A} = \left(\begin{array}{c|c} \boldsymbol{M}_{\mathrm{f}} & \boldsymbol{C}_{\mathrm{f}}^T \\ \hline \boldsymbol{C}_{\mathrm{f}} & \boldsymbol{I}_{\mathrm{f}} \end{array}\right) = -\left(\begin{array}{ccc|ccc} X_{\dot{u}} & X_{\dot{v}} & X_{\dot{w}} & X_{\dot{p}} & X_{\dot{q}} & X_{\dot{r}} \\ Y_{\dot{u}} & Y_{\dot{v}} & Y_{\dot{w}} & Y_{\dot{p}} & Y_{\dot{q}} & Y_{\dot{r}} \\ Z_{\dot{u}} & Z_{\dot{v}} & Z_{\dot{w}} & Z_{\dot{p}} & Z_{\dot{q}} & Z_{\dot{r}} \\ \hline L_{\dot{u}} & L_{\dot{v}} & L_{\dot{w}} & L_{\dot{p}} & L_{\dot{q}} & L_{\dot{r}} \\ M_{\dot{u}} & M_{\dot{v}} & M_{\dot{w}} & M_{\dot{p}} & M_{\dot{q}} & M_{\dot{r}} \\ N_{\dot{u}} & N_{\dot{v}} & N_{\dot{w}} & N_{\dot{p}} & N_{\dot{q}} & N_{\dot{r}} \end{array}\right)$$

The following table provides definitions of nondimensional quantities used to represent vis-

cous effects. These definitions largely follow the notational convention for aircraft, with some minor discrepancies (such as the use of a single characteristic length L).

Dimensional Quantity	Dimensional Divisor	Nondimensional Quantity
X, Y, Z	$\frac{1}{2}\rho V^2 S$	C_X, C_Y, C_Z
L, M, N	$\frac{1}{2}\rho V^2 S l$	C_l, C_m, C_n
u, v, w	V	$\bar{u}$, $\bar{v}$, $\bar{w}$
p, q, r	V/l	$\bar{p}$, $\bar{q}$, $\bar{r}$

Standard assumptions concerning vehicle symmetry are that the longitudinal forces and moments depend only on longitudinal state variables and the lateral-directional forces and moments depend only on lateral-directional state variables. Notation for the nondimensional stability derivatives, which characterize the viscous hydrodynamic effects, is defined below.

	C_X	C_Z	C_m
$\bar{u}$	C_{X_u}	C_{Z_u}	C_{m_u}
α	C_{X_α}	C_{Z_α}	C_{m_α}
$\bar{q}$	C_{X_q}	C_{Z_q}	C_{m_q}

	C_Y	C_l	C_n
β	C_{Y_β}	C_{l_β}	C_{n_β}
$\bar{p}$	C_{Y_p}	C_{l_p}	C_{n_p}
$\bar{r}$	C_{Y_r}	C_{l_r}	C_{n_r}

1 Introduction

1.1 Buoyancy Driven Underwater Gliders

The concept for an autonomous underwater vehicle (AUV) which uses buoyancy for propulsion was introduced in the late 1980's. These underwater gliders evolved from a special class of instrumented floats that have been used by physical oceanographers for nearly 20 years [14]. These floats, which are equipped with buoyancy actuators, can ascend and descend vertically, collecting oceanographic data along the way. Floats drift with the ocean currents, however; scientists have no control over their motion once they are released. Henry Stommel, a renowned physical oceanographer, working with his colleague Doug Webb, introduced the concept for a winged AUV with a buoyancy actuator and a moving mass for attitude control [2]. By properly modulating its net weight and attitude, this vehicle uses gravity to propel itself with tremendous efficiency. The future holds dreams of these gliders undertaking missions that can span years and travel thousands of miles performing experimental studies on the ocean environment or tracking enemy submarines in a surveillance mission [11]. Gliders are currently making historic achievements and already capable of performing a variety of solo missions. In November of 2004, a glider made history by crossing the Gulf Stream to become the first autonomous vehicle to do so [3].

The buoyancy actuator that is typically used for underwater gliders is an inflatable bladder which is exposed to the ambient ocean water. When this bladder is inflated (typically with oil), the buoyant force on the vehicle increases; when the bladder is deflated, the buoyant force on the vehicle decreases. If the vehicle is trimmed to be neutrally buoyant with the bladder half full, then modulating the bladder volume makes the vehicle rise or sink. The moving mass actuator provides attitude control in pitch and roll by moving the vehicle center of mass relative to the center buoyancy [7].

To illustrate the concept, suppose that the vehicle is in a sinking glide with a given velocity vector, V, and then inflates its bladder to become positively buoyant (i.e., light in water). As

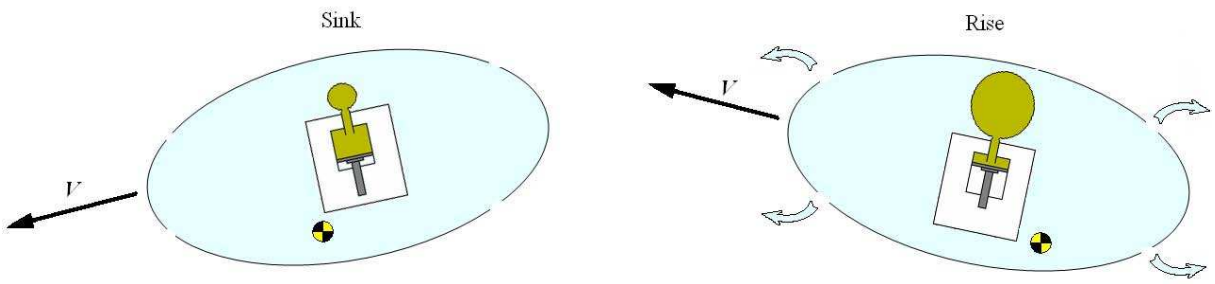

Figure 1: Exaggerated Buoyancy Engine Concept

the bladder increases, seawater (indicated by the light blue color) is pushed out of the vehicle by the increasing bladder volume. The mass of the bladder system never changes, only the volume in which it displaces. When the seawater has been pushed out of the vehicle by the increased bladder volume, the vehicle has become lighter in weight than its previous state. Suppose also that the center of mass (indicated by the yellow and black circle) is shifted rearward of the center of buoyancy so that the vehicle noses up. As the vehicle ascends, the lift generated over the fixed wing propels the vehicle forward. When the vehicle has ascended sufficiently far, the bladder is deflated and the moving mass is shifted forward. As the volume of the bladder is decreased, seawater is pulled back into the vehicle and causes the net weight of the vehicle to be heavier in weight than its previous state. The vehicle noses down and begins to descend. The lift reverses in such a way that lift continues to propel the vehicle forward, rectifying vertical motion into horizontal motion.

There are scenarios for which buoyancy driven gliders are more favorable than traditional, propeller-driven AUVs due to power storage limitations. Scenarios where buoyancy driven gliders would be more favorable would be for long-term, long-range ocean sampling tasks and also persistent surveillance tasks [5]. Gliders excel in endurance over traditional battery propulsion vehicles because their only powering needs are to inflate/deflate the buoyancy bladder and move the mass actuators which control pitch and roll. These glider powering needs are what allow the gliders to travel thousands of kilometers for many days while sampling the ocean environment [15]. Scenarios where buoyancy driven gliders would not be

favorable would be in environments with shallow water which would inhibit gliding. Further, environments with strong currents would hinder glider performance, as gliders are very slow vehicles, typically travelling at speeds near twenty-five centimeters per second [14].

The earliest three underwater gliders to be introduced are *Spray* [14], *Slocum* [15], and *Seaglider* [5]. These gliders are all designed for oceanographic observation over very long distances and durations. Although each glider is slightly different in design, the objective for each is the same: to minimize energy expended in collecting science data. The result is an ocean sampling device which can provide scientists with data that is more valuable than data from floats or moored sensors and significantly lower cost than data taken by manned research vessels.

An important capability for gliders is to navigate accurately. Model-based control design can be used to enhance navigational accuracy, but requires development of a vehicle hydrodynamic model. The primary purpose of the research in this thesis is to determine the hydrodynamic parameters that define the dynamic equations for two specific underwater gliders. The first is *Slocum* [15]. *Slocum*, named for Joshua Slocum who was the first person to sail around the world alone, has a traditional airplane shape: a cylindrical fuselage, swept wings, and a vertical tail fin, which is connected to the fuselage by a tail boom. While a vertical tail is necessary for directional stability, a horizontal tail is not necessary for a sufficiently bottom-heavy vehicle. *Slocum* is a medium-sized glider with an overall length of 3.2 meters, a fuselage diameter of 0.165 meters, and a displaced mass of 40 kilograms. The glider can travel to a depth of 2600 meters and has a stated operational range of approximately 40,000 kilometers [15]. The second glider considered in this thesis is *XRay/Liberdade*, a blended wing-body underwater glider designed and built by a team from the Scripps Institute of Oceanography's Marine Physical Laboratory and the University of Washington's Applied Physics Laboratory [8].

The hydrodynamic parameters which define the dynamic equations for an underwater glider can be categorized into viscous terms and inviscid terms. Viscous terms are those param-

eters that depend on viscous drag and lift over the body, in aggregate, or over individual components of the body. Inviscid terms are those parameters which arise from potential flow theory, such as added mass and added inertia. For generic aircraft shapes, such as *Slocum*, there are well-used semi-empirical tools for estimating the viscous terms. For less traditional shapes, such as *XRay/Liberdade*, the tools for estimating viscous terms are not so well-developed. In neither case are there reliable analytical or semi-empirical methods for determining the inviscid terms. To compute these terms requires solving Laplace's equation with complicated boundary conditions, a task which must generally be done numerically. This thesis describes semi-empirical and numerical methods used to estimate the viscous and inviscid terms appearing in the dynamic equations for *Slocum*. It also describes the numerical computation of inviscid terms for *XRay/Liberdade*. In addition, since the capability and expertise to compute added mass and added inertia for complicated shapes has been developed, the thesis also describes hydrodynamic model development for the 4.75 inch diameter Virginia Tech Miniature AUV (475).

1.2 Standard Modeling Methods

There are several methods that will produce results for hydrodynamic parameters based on a given geometry. The methods include analytical, experimental, computational, and semi-empirical approaches. The distinctions between the modeling methods are further described below.

Analytical methods for determining model parameter values include implementing strip theory or solving Laplace's equation. Strip theory, also known as slender body approximation, can be applied to slender bodies in order to estimate the hydrodynamic parameters (such as added mass and inertia) for a body using the 2D sectional properties. Strip theory can also approximate other parameters in the equations of motion, such as damping coefficients. One assumption of strip theory is that the vessel is slender. Slender vessels have a small beam (or draft)-to-length ratio, meaning any cross-sectional changes occur gradually over the

length of the vessel. Strip theory takes the hydrodynamic parameters of the 2D shape and integrates the parameters over the length of the vessel. Another assumption of strip theory is that there are small angle changes in the vehicle's maneuver. For the *Slocum* glider, strip theory may be appropriately used since the glider can be assumed to be slender. However, for the *XRay/Liberdade*, strip theory cannot provide an approximation for the hydrodynamic parameters. In both glider cases, the small angle change assumption is generally reasonable.

Another approach to determining the mathematical model parameters is to do experimental studies. These studies include sea trials and tow-tank tests. These methods are costly due to the expense of constructing scale vehicle models and operating the experimental facility. Further, the added mass and inertia terms are difficult to obtain from sea trials.

A third approach to determining the mathematical model parameters is to use computational methods. Computational fluid dynamics (CFD) involves solving the Navier-Stokes flow equations numerically using a computer. CFD programs are less costly than tow-tank and sea trial testing and more broadly applicable than analytical methods, however they require an expert to grid the model and validate the results. CFD programs can handle any type of trajectory that one would prescribe for the model, making this a viable approach for determining difficult-to-measure model parameters for the *Slocum* and *XRay/Liberdade* gliders. CFD programs are generally validated using experimental data from wind tunnel tests. Today, there is a large number of different CFD programs available, each with its own advantages and disadvantages. For each of these codes, a user defines a geometry, generates a grid pattern over the geometry, then applies the particular algorithm developed for that CFD program.

One final method for determining model parameters is to use a semi-empirical approach. Semi-empirical approaches use experimentally derived guidelines for estimating model parameter values for vehicles with generic shapes.

1.3 Proposed Approach

The approach followed in this thesis in order to determine the hydrodynamic properties involves several steps. To solve for the inviscid parameters, a commercially available CFD program called USAERO was used for the vehicles to perform computational flight tests, as described in Section 3.2. USAERO is used to solve for the inviscid coefficients by solving Laplace's equations. Semi-empirical computations are performed on the same models using USAF DatCom [4] and Roskam [13] to solve for the viscous parameters. In addition to these sources, additional information required to complete the hydrodynamic parameters, such as rigid body data, is obtained using the 3D modeling software Rhinoceros 3.0.

2 Mathematical Modeling

An objective of this research is to provide parameter values for the dynamic equations that will describe an underwater glider's motion. This section develops the general equations.

2.1 Reference Frames

Reference frames must be defined before an analysis of the kinematic and dynamic equations can be made. The moving coordinate frame ($\boldsymbol{b}$) and the fixed-in-space inertial frame ($\boldsymbol{i}$) are shown in Figure 2.

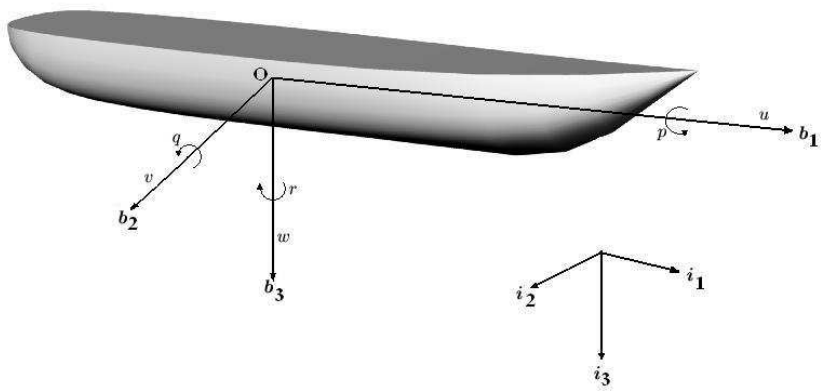

Figure 2: Reference Frames

Here, 'O' is the origin of the body-fixed frame, which in this study coincides with the center of volume of the model, as determined from Rhinoceros 3.0. The variables listed in Figure 2 are explained in Table 1.

The motion of the body-fixed frame is described relative to the inertial frame. Following the notation from [6], the model's position and orientation can be expressed relative to the inertial frame by $\boldsymbol{\eta_1} = [x, y, z]^T$ and $\boldsymbol{\eta_2} = [\phi, \theta, \psi]^T$, respectively. Here, x, y, and z refer to the position of the body with respect to the inertial frame. The variables ϕ, θ, and ψ refer to the angular orientation of the body with respect to the inertial frame in roll, pitch,

Table 1: SNAME notation for for marine vessels; see [6].

Degree of Freedom	forces/moments	linear/angular velocities
Translation along x-axis (surge)	X	u
Translation along y-axis (sway)	Y	v
Translation along z-axis (heave)	Z	w
Rotation about x-axis (roll)	L	p
Rotation about y-axis (pitch)	M	q
Rotation about z-axis (yaw)	N	r

and yaw, respectively. The linear and angular velocity with respect to the inertial frame are expressed in the body frame as $\boldsymbol{\nu_1} = [u, v, w]^T$ and $\boldsymbol{\nu_2} = [p, q, r]^T$, respectively.

2.2 Kinematics

Consider the case presented in Figure 3 where the two reference frames shown in Figure 2 share the same origin. One way to express the body frame unit vectors in the inertial frame is through projection.

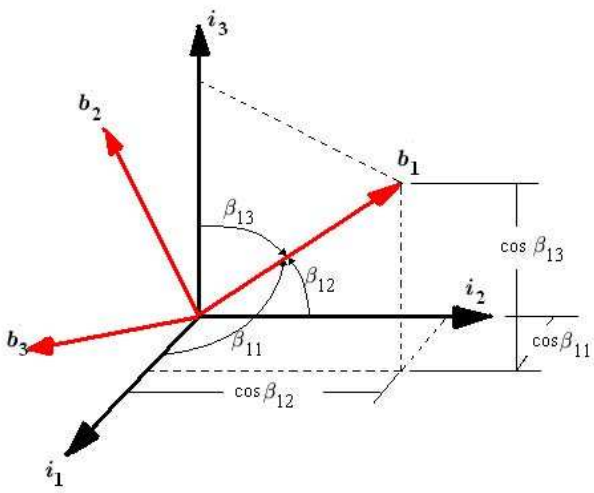

Figure 3: Direction Cosines - Projection of $\boldsymbol{b_1}$ onto $\{\boldsymbol{i}\}$

Expressing the body frame unit vector, $\boldsymbol{b_1}$, as a projection to the inertial frame yields the following equation,

$$\boldsymbol{b_1} = \cos\beta_{11}\boldsymbol{i_1} + \cos\beta_{12}\boldsymbol{i_2} + \cos\beta_{13}\boldsymbol{i_3} \tag{1}$$

Similarly, this can be done for the other two remaining unit vectors in the body frame.

$$\boldsymbol{b_2} = \cos\beta_{21}\boldsymbol{i_1} + \cos\beta_{22}\boldsymbol{i_2} + \cos\beta_{23}\boldsymbol{i_3} \tag{2}$$

$$\boldsymbol{b_3} = \cos\beta_{31}\boldsymbol{i_1} + \cos\beta_{32}\boldsymbol{i_2} + \cos\beta_{33}\boldsymbol{i_3} \tag{3}$$

These equations can be put into vector and matrix form in the following manner.

$$\{\boldsymbol{b}\} = \begin{bmatrix} \cos\beta_{11} & \cos\beta_{12} & \cos\beta_{13} \\ \cos\beta_{21} & \cos\beta_{22} & \cos\beta_{23} \\ \cos\beta_{31} & \cos\beta_{32} & \cos\beta_{33} \end{bmatrix} \{\boldsymbol{i}\} = [\boldsymbol{R}]\{\boldsymbol{i}\} \tag{4}$$

Here, $[\boldsymbol{R}]$ is known as the direction cosine matrix. This direction cosine matrix can be parameterized in terms of the Euler angles, roll, pitch, and yaw, described above. In airplane and underwater glider applications, it is popular to choose an Euler angle rotation through the roll angle, ϕ, the pitch angle, θ, and the yaw angle, ψ. Given a specified Euler angle, three direction cosine matrices are used to relate the body frame to the inertial frame. Define planar rotation matrices,

$$[\boldsymbol{R_1}(\theta)] = \begin{bmatrix} 1 & 0 & 0 \\ 0 & \cos\theta & -\sin\theta \\ 0 & \sin\theta & \cos\theta \end{bmatrix} \tag{5}$$

$$[\boldsymbol{R_2}(\theta)] = \begin{bmatrix} \cos\theta & 0 & \sin\theta \\ 0 & 1 & 0 \\ -\sin\theta & 0 & \cos\theta \end{bmatrix} \tag{6}$$

$$[\boldsymbol{R_3}(\theta)] = \begin{bmatrix} \cos\theta & -\sin\theta & 0 \\ \sin\theta & \cos\theta & 0 \\ 0 & 0 & 1 \end{bmatrix} \tag{7}$$

The direction cosine matrix, $\boldsymbol{R}(\phi, \theta, \psi)$, which maps free vectors from the body frame to the inertial frame is

$$[\boldsymbol{R}(\phi, \theta, \psi)] = [\boldsymbol{R_3}(\psi)][\boldsymbol{R_2}(\theta)][\boldsymbol{R_1}(\phi)] \tag{8}$$

which can be restated as,

$$[\boldsymbol{R}(\eta_2)] = \begin{bmatrix} \cos\psi\cos\theta & -\sin\psi\cos\phi + \cos\psi\sin\theta\sin\phi & \sin\psi\sin\phi + \cos\psi\cos\phi\sin\theta \\ \sin\psi\cos\theta & \cos\psi\cos\phi + \sin\phi\sin\theta\sin\psi & -\cos\psi\sin\phi + \sin\theta\sin\psi\cos\phi \\ -\sin\theta & \cos\theta\sin\phi & \cos\theta\cos\phi \end{bmatrix} \tag{9}$$

The Euler angular rates, $\dot{\boldsymbol{\eta}}_{\boldsymbol{2}}$ are defined by the body angular rate and the attitude of the body frame.

$$\dot{\boldsymbol{\eta}}_{\boldsymbol{2}} = [\boldsymbol{R_2}(\boldsymbol{\eta_2})]\boldsymbol{\nu_2} \tag{10}$$

The transformation matrix, $\boldsymbol{R_2}(\boldsymbol{\eta_2})$, can be derived through,

$$\dot{\boldsymbol{\eta}}_{\mathbf{2}} = \begin{bmatrix} \dot{\phi} \\ 0 \\ 0 \end{bmatrix} + [\boldsymbol{R}_{\mathbf{1}}(\phi)]^T \begin{bmatrix} 0 \\ \dot{\theta} \\ 0 \end{bmatrix} + [\boldsymbol{R}_{\mathbf{1}}(\phi)]^T [\boldsymbol{R}_{\mathbf{2}}(\theta)]^T \begin{bmatrix} 0 \\ 0 \\ \dot{\psi} \end{bmatrix} = [\boldsymbol{R}_{\mathbf{2}}(\boldsymbol{\eta}_{\mathbf{2}})]^{-1} \dot{\boldsymbol{\eta}}_{\mathbf{2}} \tag{11}$$

Expanding Equation (11) and taking the inverse, we can state the proper transformation matrix which relates the body-fixed angular velocity and the Euler rate vector as,

$$[\boldsymbol{R}_{\mathbf{2}}(\boldsymbol{\eta}_{\mathbf{2}})] = \begin{bmatrix} 1 & \sin\phi\tan\theta & \cos\phi\tan\theta \\ 0 & \cos\psi & -\sin\phi \\ 0 & \sin\phi/\cos\theta & \cos\phi/\cos\theta \end{bmatrix} \tag{12}$$

There is a singularity at $\theta = \pm\pi/2$ in Equation 12. In applications where this may be a problem, another possibility is to use the quaternion representation. Summarizing the results from Section 2.2 yields Equation (13), which expresses the kinematic equations in vector form.

$$\begin{bmatrix} \dot{\boldsymbol{\eta}}_{\mathbf{1}} \\ \dot{\boldsymbol{\eta}}_{\mathbf{2}} \end{bmatrix} = \begin{bmatrix} \boldsymbol{R}_{\mathbf{1}}(\boldsymbol{\eta}_{\mathbf{2}}) & 0_{3\times3} \\ 0_{3\times3} & \boldsymbol{R}_{\mathbf{2}}(\boldsymbol{\eta}_{\mathbf{2}}) \end{bmatrix} \begin{bmatrix} \boldsymbol{\nu}_{\mathbf{1}} \\ \boldsymbol{\nu}_{\mathbf{2}} \end{bmatrix} \tag{13}$$

2.3 Dynamics

Linear momentum, $\boldsymbol{p}$, and angular momentum, $\boldsymbol{h}$, are used to define the dynamic equations of motion. These two momentum vectors are the conjugate momenta corresponding to $\boldsymbol{\nu}_{\mathbf{1}}$ and $\boldsymbol{\nu}_{\mathbf{2}}$, respectively. To develop the expressions for $\boldsymbol{p}$ and $\boldsymbol{h}$ requires several definitions.

The inertia matrix, $\boldsymbol{I}$, is composed of three separate inertia matrices: the added inertia matrix, $\boldsymbol{I}_{\mathbf{f}}$ and the rigid body inertia matrix, $\boldsymbol{I}_{\mathbf{rb}}$. $\boldsymbol{I}_{\mathbf{f}}$ accounts for the added inertia of the system as the fluid is accelerated when the body is rotated. $\boldsymbol{I}_{\mathbf{rb}}$ accounts for the inertia due to the defined geometry of the model and the inertia caused by the moving mass which helps control the vehicle in a maneuver. If the underwater glider's external geometry is such that

the $\boldsymbol{b_1}$-$\boldsymbol{b_2}$ and $\boldsymbol{b_1}$-$\boldsymbol{b_3}$ planes are planes of symmetry, the added inertia matrix is diagonal [10]. The added inertia of the system is,

$$\boldsymbol{I_{\mathbf{f}}} = -\text{diag}\begin{pmatrix} L_{\dot{p}} & M_{\dot{q}} & N_{\dot{r}} \end{pmatrix} \tag{14}$$

where $L_{\dot{p}}$, $M_{\dot{q}}$, and $N_{\dot{r}}$ are defined as roll moment due to roll acceleration, pitch moment due to pitch acceleration, and yaw moment due to yaw acceleration, respectively [6]. For typical underwater glider configurations, the rigid body inertia matrix takes the form,

$$\boldsymbol{I_{\mathbf{rb}}} = \begin{pmatrix} I_{xx} & 0 & -I_{xz} \\ 0 & I_{yy} & 0 \\ -I_{xz} & 0 & I_{zz} \end{pmatrix} - m_p \hat{\boldsymbol{r}}_{\boldsymbol{p}} \hat{\boldsymbol{r}}_{\boldsymbol{p}} \tag{15}$$

where I_{xz} appears when the center of mass is not located on a body frame axis. Here, m_p is the mass of the control moving mass. The vector $\boldsymbol{r_p}$ is the vector from the location of the center of mass to the location of the control moving mass. The 3×3 matrix $\hat{\boldsymbol{r}}_{\boldsymbol{p}}$ is defined as the skew-symmetric cross-product equivalent matrix formed from the particle location vector, $\boldsymbol{r_p}$.

$$\hat{\boldsymbol{r}}_{\boldsymbol{p}} = \begin{pmatrix} 0 & -r_{p3} & r_{p2} \\ r_{p3} & 0 & -r_{p1} \\ -r_{p2} & r_{p1} & 0 \end{pmatrix} \tag{16}$$

We assume that the vehicle center of mass is located in the $\boldsymbol{b_1}$-$\boldsymbol{b_3}$ plane, and we assume that $\boldsymbol{r_p} = r_p \boldsymbol{b_2}$. Combining the three matrices together yields,

$$\boldsymbol{I} = \boldsymbol{I_{\mathbf{f}}} + \boldsymbol{I_{\mathbf{rb}}} \tag{17}$$

The next definition is for the mass matrix, $\boldsymbol{M}$, of the system. The mass matrix is the sum of two matrices; the added mass matrix, $\boldsymbol{M_{\mathbf{f}}}$, and the vehicle mass matrix, $\boldsymbol{M_v}$. Like the

added inertia matrix, the added mass matrix is diagonal for the gliders considered here due to their planes of symmetry.

$$\boldsymbol{M_{\mathbf{f}}} = -\text{diag}\begin{pmatrix} X_{\dot{u}} & Y_{\dot{v}} & Z_{\dot{w}} \end{pmatrix} \tag{18}$$

where $X_{\dot{u}}$, $Y_{\dot{v}}$, and $Z_{\dot{w}}$ are the force in the x-direction due to acceleration in the x-direction, force in the y-direction due to acceleration in the y-direction, and force in the z-direction due to acceleration in the z-direction, respectively [6]. The vehicle mass matrix is defined as,

$$\boldsymbol{M_{\mathbf{rb}}} = \begin{pmatrix} m_v & 0 & 0 \\ 0 & m_v & 0 \\ 0 & 0 & m_v \end{pmatrix} = m_v \mathbb{I} \tag{19}$$

Here, m_v is the mass of the rigid body vehicle and $\mathbb{I}$ is the 3x3 identity matrix. Combining the two matrices yields,

$$\boldsymbol{M} = \boldsymbol{M_{\mathbf{f}}} + \boldsymbol{M_{\mathbf{rb}}} \tag{20}$$

The coupling matrix, C, arises from the potential flow and inertial coupling between the translational and rotational kinetic energy of the system. There are two components in the coupling matrix. The added coupling matrix, $\boldsymbol{C_{\mathbf{f}}}$ is defined as,

$$\boldsymbol{C_{\mathbf{f}}} = -\begin{pmatrix} 0 & 0 & 0 \\ 0 & 0 & M_{\dot{w}} \\ 0 & N_{\dot{v}} & 0 \end{pmatrix} = -\begin{pmatrix} 0 & 0 & 0 \\ 0 & 0 & Y_{\dot{r}} \\ 0 & Z_{\dot{q}} & 0 \end{pmatrix}^T \tag{21}$$

where $M_{\dot{w}}$ and $N_{\dot{v}}$ are the pitch moment due to acceleration in the z-direction, and yaw moment due to acceleration in the y-direction, respectively. $Y_{\dot{r}}$ and $Z_{\dot{q}}$ are the side force due to yaw acceleration, and lift force due to pitch acceleration, respectively. It is important

to note that Equation (21) refers to models with two planes of symmetry. The rigid body matrix is defined as,

$$\boldsymbol{C}_{\mathbf{rb}} = m_v \hat{r}_{rb} + m_p \hat{r}_p = -\boldsymbol{C}_{\mathbf{rb}}^{\boldsymbol{T}} \tag{22}$$

Combining the two components yields the equation for the coupling matrix,

$$\boldsymbol{C} = \boldsymbol{C}_{\mathbf{f}} + \boldsymbol{C}_{\mathbf{rb}} \tag{23}$$

To determine expressions for the linear and angular momentum, $\boldsymbol{p}$ and $\boldsymbol{h}$, one must write the kinetic energy,

$$\boldsymbol{T} = \frac{1}{2}\boldsymbol{\nu}^T \boldsymbol{M}_{\boldsymbol{GIM}} \boldsymbol{\nu} \tag{24}$$

where $\boldsymbol{M}_{\boldsymbol{GIM}}$ is the generalized inertia matrix for the system. For this system, the kinetic energy can be written as a summation of the rigid body kinetic energy and the fluid added mass/inertia kinetic energy. The complete kinetic energy of the body/fluid system is,

$$\begin{aligned}
\boldsymbol{T} &= \boldsymbol{T}_{\mathbf{rb}} + \boldsymbol{T}_{\mathbf{f}} && (25)\\
&= \frac{1}{2}\begin{pmatrix} \boldsymbol{\nu_1} \\ \boldsymbol{\nu_2} \end{pmatrix}^T \begin{pmatrix} \boldsymbol{M}_{\mathbf{rb}} & \boldsymbol{C}_{\mathbf{rb}}^{\boldsymbol{T}} \\ \boldsymbol{C}_{\mathbf{rb}} & \boldsymbol{I}_{\mathbf{rb}} \end{pmatrix} \begin{pmatrix} \boldsymbol{\nu_1} \\ \boldsymbol{\nu_2} \end{pmatrix} + \frac{1}{2}\begin{pmatrix} \boldsymbol{\nu_1} \\ \boldsymbol{\nu_2} \end{pmatrix}^T \begin{pmatrix} \boldsymbol{M}_{\mathbf{f}} & \boldsymbol{C}_{\mathbf{f}}^{\boldsymbol{T}} \\ \boldsymbol{C}_{\mathbf{f}} & \boldsymbol{I}_{\mathbf{f}} \end{pmatrix} \begin{pmatrix} \boldsymbol{\nu_1} \\ \boldsymbol{\nu_2} \end{pmatrix} && (26)\\
&= \frac{1}{2}\begin{pmatrix} \boldsymbol{\nu_1} \\ \boldsymbol{\nu_2} \end{pmatrix}^T \begin{pmatrix} \boldsymbol{M} & \boldsymbol{C}^{\boldsymbol{T}} \\ \boldsymbol{C} & \boldsymbol{I} \end{pmatrix} \begin{pmatrix} \boldsymbol{\nu_1} \\ \boldsymbol{\nu_2} \end{pmatrix} && (27)
\end{aligned}$$

Linear and angular momentum are defined as,

$$\begin{pmatrix} \boldsymbol{p} \\ \boldsymbol{h} \end{pmatrix} = \begin{pmatrix} \partial \boldsymbol{T}/\partial \boldsymbol{\nu_1} \\ \partial \boldsymbol{T}/\partial \boldsymbol{\nu_2} \end{pmatrix} = \begin{pmatrix} \boldsymbol{M} & \boldsymbol{C^T} \\ \boldsymbol{C} & \boldsymbol{I} \end{pmatrix} \begin{pmatrix} \boldsymbol{\nu_1} \\ \boldsymbol{\nu_2} \end{pmatrix} \tag{28}$$

The dynamic equations relate the change of linear and angular momentum to external forces and moments. The dynamic equations of motion are,

$$\dot{\boldsymbol{p}} = \boldsymbol{p} \times \boldsymbol{\nu_2} + \tilde{m}g \left(\boldsymbol{R_1}(\boldsymbol{\eta_2})^T \boldsymbol{i}_3 \right) + \boldsymbol{F}_{\text{viscous}} \tag{29}$$

$$\dot{\boldsymbol{h}} = \boldsymbol{h} \times \boldsymbol{\nu_2} + \boldsymbol{p} \times \boldsymbol{\nu_1} + (m_{\text{p}} g \boldsymbol{r}_{\text{p}} + m_{\text{rb}} g \boldsymbol{r}_{\text{rb}}) \times \left(\boldsymbol{R_1}(\boldsymbol{\eta_2})^T \boldsymbol{i}_3 \right) + \boldsymbol{M}_{\text{viscous}}. \tag{30}$$

Here, $\tilde{m}$ refers the system's net mass which is modulated by inflatable bladders which change their volume and cause the vehicle to sink or rise due to net buoyancy. $\boldsymbol{F}_{\text{viscous}}$ and $\boldsymbol{M}_{\text{viscous}}$ refer to external forces and moments, respectively, that do not result from scalar potential functions. These values include viscous forces and control moments which are explored in Section A using semi-empirical methods. The equations for the viscous forces and moments are as follows,

$$\boldsymbol{F}_{\text{viscous}} = -[\boldsymbol{R_{BC}}(\alpha, \beta)] \begin{pmatrix} \mathcal{D}(\alpha) \\ \mathcal{S}_\beta \beta + \mathcal{S}_{\delta r} \delta r \\ \mathcal{L}_\alpha \alpha \end{pmatrix} \tag{31}$$

where $\boldsymbol{R_{BC}}(\alpha, \beta)$ is the proper rotation matrix that transforms the free vectors from the current frame to the body frame. $\mathcal{D}$, $\mathcal{S}$, and $\mathcal{L}$ refer to the drag, sideslip, and lift values of the system and will be developed further later.

$$\boldsymbol{M}_{\text{viscous}} = \boldsymbol{D_\omega} \boldsymbol{\nu_2} + \begin{pmatrix} L_\beta \beta \\ M_\alpha \alpha \\ N_\beta \beta + N_{\delta r} \delta r \end{pmatrix} \tag{32}$$

Here, the $\boldsymbol{D_\omega}$ matrix contains terms which characterize viscous angular damping (such as pitch and yaw damping). We assume the roll and yaw damping are decoupled.

$$\boldsymbol{D_\omega} = [(1/4)\rho V S l^2] \cdot \mathrm{diag}(C_{l_p}, C_{m_q}, C_{n_r}) \tag{33}$$

Expressions for $C_{l_p}, C_{m_q}, C_{n_r}$ are developed in Section A.3. Other useful equations that relate the viscous coefficients, which can be stated from [10], are as follows. The components of viscous force are,

$$\mathcal{D}(\alpha) = [(1/2)\rho V^2 S] C_D(\alpha) \tag{34}$$

$$\mathcal{S}(\beta) = [(1/2)\rho V^2 S] C_S(\beta) \tag{35}$$

$$\mathcal{L}(\alpha) = [(1/2)\rho V^2 S] C_L(\alpha) \tag{36}$$

where,

$$C_D(\alpha) = C_{D_0} + \kappa C_L(\alpha)^2 \tag{37}$$

$$C_S(\beta) = C_{S_\beta}\beta \tag{38}$$

$$C_L(\alpha) = C_{L_\alpha}\alpha \tag{39}$$

The components of viscous moment are,

$$L_\beta \beta = [(1/2)\rho V^2 Sl] C_{l_\beta} \beta \tag{40}$$

$$M_\alpha \alpha = [(1/2)\rho V^2 Sl] C_{m_\alpha} \alpha \tag{41}$$

$$N_\beta \beta + N_{\delta r} \delta r = [(1/2)\rho V^2 Sl](C_{n_\beta} \beta + C_{n_{\delta r}} \delta r) \tag{42}$$

These forces and moments are assumed to be linear due to the small angle changes experienced in flight. Expressions for all of the non-dimensional coefficients (C_{m_α}, C_{n_β}, $C_{n_{\delta r}}$, etc.) are developed in Appendix A.3; the values are summarized in Table 8.

2.4 Math Modeling Summary

This research aims to compute underwater glider model parameters appearing in the dynamic equations (29) and (30). A CFD program, USAERO, is used to generate the added mass/inertia and coupling values, $\boldsymbol{M}_{\mathbf{f}}$, $\boldsymbol{C}_{\mathbf{f}}$, and $\boldsymbol{I}_{\mathbf{f}}$. Other parameters, such as $\boldsymbol{I}_{\mathbf{rb}}$, $\boldsymbol{M}_{\mathbf{rb}}$, $\boldsymbol{C}_{\mathbf{rb}}$, etc. can be determined from Rhinoceros 3.0 and by knowing the weight and location the vehicle particle moving mass.

A semi-empirical approach is used to determine the viscous forces and moments, $\boldsymbol{F}_{\text{viscous}}$ and $\boldsymbol{M}_{\text{viscous}}$, in Equations (31) and (32). In this thesis, the viscous parameters were obtained for *Slocum* only.

3 Inviscid Coefficients from Computational Flight Tests

We derive the inviscid hydrodynamic parameters through unsteady "computational flight tests" using a commerical CFD program known as USAERO. This section explains the origins of USAERO and the approach used in determining these hydrodynamic parameters. It details the validation of the software and provides the final results obtained.

3.1 Motivation

The inviscid parameters that we are trying to solve for are the added mass/inertia and coupling terms that result when a body is accelerated through a fluid at rest. In Section 2.3 we referenced these parameters in their matrix form and showed how they fit into the equations of motion, but have not yet discussed how to obtain them.

Suppose we had a way of accelerating a body within a fluid at rest. From this experiment we would find that under a constant acceleration, a constant force and/or moment is generated. If we had a method of studying a vehicle under several different values of constant acceleration, we could present the results as in Figure 4.

Acceleration is graphed on the x-axis and the resulting force (or moment) is graphed on the y-axis. The lines represent the different forces and moments due to varying constant accelerations in one direction, in this case the x-direction. Performing linear curve fits to these data reveals the slopes of the lines. These slopes are the values that we are after. Once we have solved for these slopes, we may populate the matrix given in Equation (43).

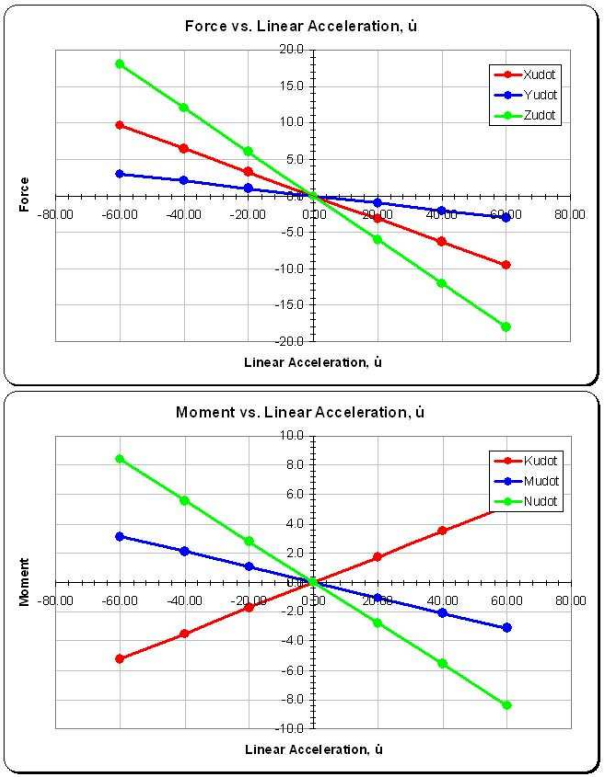

Figure 4: Forces and moments due to constant accelerations in the x-direction

$$\boldsymbol{M_A} = \left(\begin{array}{c|c} \boldsymbol{M}_{\mathrm{f}} & \boldsymbol{C}_{\mathrm{f}}^T \\ \hline \boldsymbol{C}_{\mathrm{f}} & \boldsymbol{I}_{\mathrm{f}} \end{array}\right) = -\left(\begin{array}{ccc|ccc} X_{\dot{u}} & X_{\dot{v}} & X_{\dot{w}} & X_{\dot{p}} & X_{\dot{q}} & X_{\dot{r}} \\ Y_{\dot{u}} & Y_{\dot{v}} & Y_{\dot{w}} & Y_{\dot{p}} & Y_{\dot{q}} & Y_{\dot{r}} \\ Z_{\dot{u}} & Z_{\dot{v}} & Z_{\dot{w}} & Z_{\dot{p}} & Z_{\dot{q}} & Z_{\dot{r}} \\ \hline L_{\dot{u}} & L_{\dot{v}} & L_{\dot{w}} & L_{\dot{p}} & L_{\dot{q}} & L_{\dot{r}} \\ M_{\dot{u}} & M_{\dot{v}} & M_{\dot{w}} & M_{\dot{p}} & M_{\dot{q}} & M_{\dot{r}} \\ N_{\dot{u}} & N_{\dot{v}} & N_{\dot{w}} & N_{\dot{p}} & N_{\dot{q}} & N_{\dot{r}} \end{array}\right) \tag{43}$$

$X_{\dot{u}}$, for example, comes from the slope of the line that results from graphing the force in the x-direction (X) due to a linear acceleration in the x-direction ($\dot{u}$). The units on this added inertia matrix, $\boldsymbol{M_A}$, presented in this thesis are as follows: the upper-left three by three added mass matrix is in slugs, the lower-left and upper-right three by three added coupling matrices are in slugs·feet, and the lower-right three by three added inertia matrix

is in slugs·feet^2.

3.2 USAERO to Compute Inviscid Parameters

USAERO is an unsteady version of the commercially available program VSAERO which was developed for NASA Langley Research Center in 1978 [1]. The development of USAERO was sponsored by the Office of Naval Research (ONR) to support submarine maneuvering predictions that required analysis of unsteady motion and inviscid effects. USAERO has the ability to compute the unsteady flow characteristics for single or multiple bodies in general motion, or at rest in a moving fluid. It uses a time-stepping approach that solves a surface singularity model using quadrilateral panels of uniformly distributed doublets and sources. USAERO has the capability to output several different types of calculated results, including the integrated force and moment histories on a body.

One assumption that USAERO makes that was mentioned in Section 1.2 is that the effects of viscosity are largely confined to a thin boundary layer on the body surface. This allows the majority of flow to be classified as inviscid. USAERO is not intended to solve the complete Navier-Stokes equations. Using flow theory, the doublets and sources are solved over the time history for the body, which allows for surface velocities and pressures to be evaluated. This in turn allows the pressure coefficient on each panel to be computed. With the pressure coefficient and velocity of each surface point evaluated, the force and moment acting on the body can be computed by integrating the pressure over the surface.

USAERO is also capable of wake studies, flow tracing, internal flow, and propulsor modeling. However, for this research, the only necessary techniques and methods are those which yield the force and moment coefficients.

USAERO has the ability to analyze a body over a given time frame within a defined flow and to determine the forces and moments acting on the body. Further, USAERO has the ability to simulate a body accelerating in a flow and obtain any forces and moments due

to the acceleration. These forces and moments due to acceleration are the desired output of USAERO for this research. The body is defined and oriented in USAERO, then given a constant acceleration in a particular degree of freedom (surge, heave, sway, yaw, pitch, or roll). Given the prescribed constant acceleration and the resulting forces and moments on the body, one may graph force due to acceleration. Solving for the slope of the line generated by this analysis yields the added mass/inertia term.

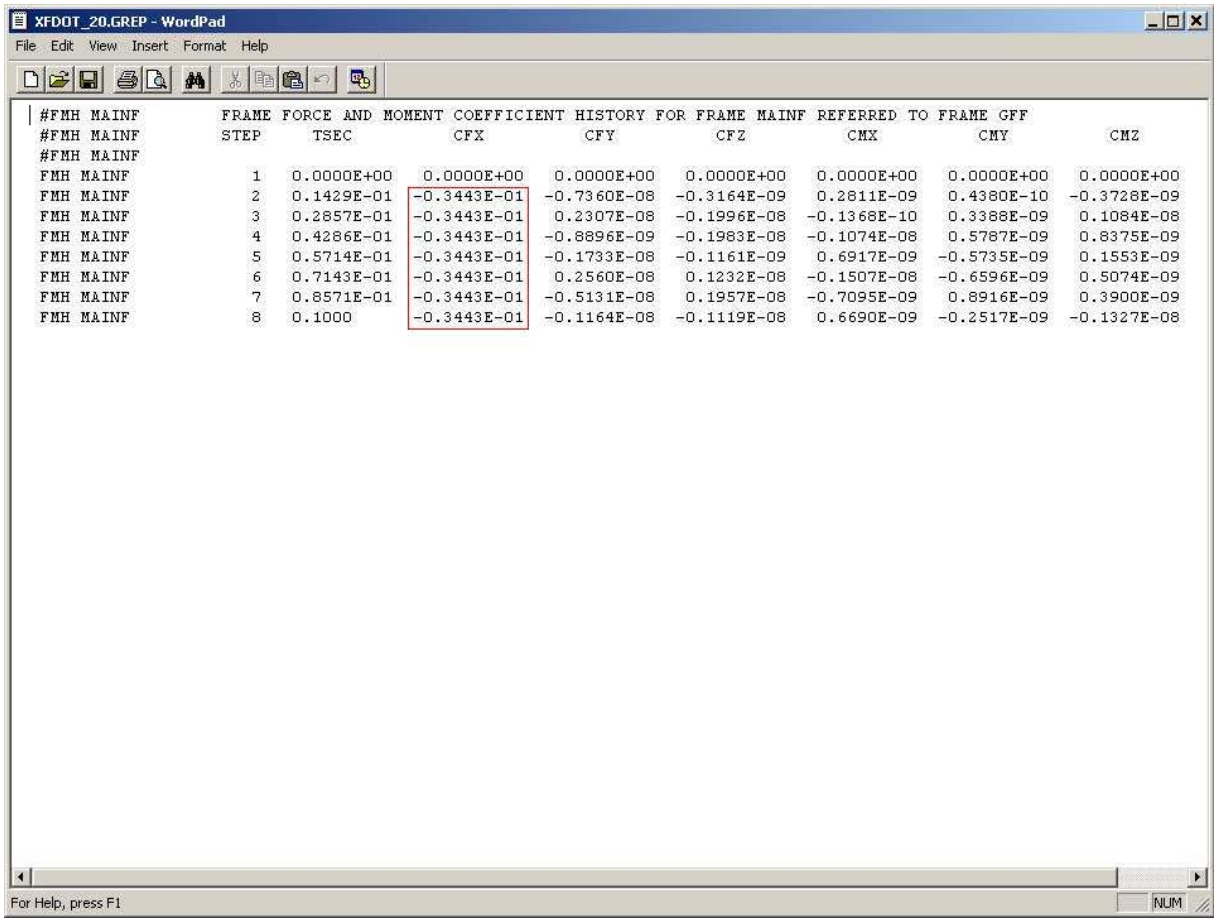

XFDOT_20.GREP - WordPad

File Edit View Insert Format Help

#FMH MAINF FRAME FORCE AND MOMENT COEFFICIENT HISTORY FOR FRAME MAINF REFERRED TO FRAME GFF

#FMH MAINF	STEP	TSEC	CFX	CFY	CFZ	CMX	CMY	CMZ
#FMH MAINF								
FMH MAINF	1	0.0000E+00	0.0000E+00	0.0000E+00	0.0000E+00	0.0000E+00	0.0000E+00	0.0000E+00
FMH MAINF	2	0.1429E-01	-0.3443E-01	-0.7360E-08	-0.3164E-09	0.2811E-09	0.4380E-10	-0.3728E-09
FMH MAINF	3	0.2857E-01	-0.3443E-01	0.2307E-08	-0.1996E-08	-0.1368E-10	0.3388E-09	0.1084E-08
FMH MAINF	4	0.4286E-01	-0.3443E-01	-0.8896E-09	-0.1983E-08	-0.1074E-08	0.5787E-09	0.8375E-09
FMH MAINF	5	0.5714E-01	-0.3443E-01	-0.1733E-08	-0.1161E-09	0.6917E-09	-0.5735E-09	0.1553E-09
FMH MAINF	6	0.7143E-01	-0.3443E-01	0.2560E-08	0.1232E-08	-0.1507E-08	-0.6596E-09	0.5074E-09
FMH MAINF	7	0.8571E-01	-0.3443E-01	-0.5131E-08	0.1957E-08	-0.7095E-09	0.8916E-09	0.3900E-09
FMH MAINF	8	0.1000	-0.3443E-01	-0.1164E-08	-0.1119E-08	0.6690E-09	-0.2517E-09	-0.1327E-08

For Help, press F1 NUM

Figure 5: Constant Force Coefficient in x-direction due to acceleration in x-direction for 5 ft Radius Sphere

Figure 5 shows an example of the output file generated by USAERO. Figure 5 comes from a test case that will be described in Section 3.4.1 that had an acceleration of 20 ft/s^2 in the x-direction. The point of interest in Figure 5 is the constant force coefficient in the x-

direction (CFX) due to an acceleration in the x-direction. With multiple acceleration cases, and knowing that at zero acceleration there will be zero forces and moments on the vehicle, there are sufficient data points to generate a graph showing the variation in force or moment coefficients due to changes in acceleration.

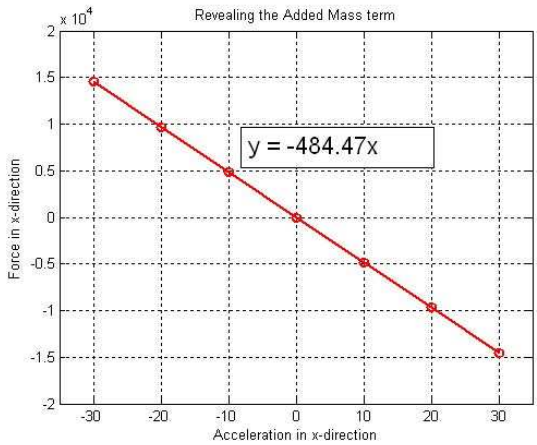

Figure 6: Computing $X_{\dot{u}}$ for a sphere with a 5 ft radius.

Figure 6 shows force on the y-axis and acceleration (in one degree of freedom) on the x-axis for a sphere with a five foot radius. Fitting a linear curve to this graph reveals the added mass term as the slope of the fitted linear curve. The slope of the linear curve fit in Figure 6 is -484.47 slugs, which is the added mass term of $X_{\dot{u}}$ as calculated through USAERO. Note that, because of spherical symmetry, no other forces and moments result from an x-axis acceleration. The same series of acceleration cases are performed for $\dot{v}$, $\dot{w}$, $\dot{p}$, $\dot{q}$, and $\dot{r}$ allowing for the added mass/added inertia and coupling matrix to be computed.

3.2.1 USAERO Calculation Discussion

The Navier-Stokes equations are nonlinear partial differential equations that can help describe the motion of a fluid. The equations are formed from the conservation of momentum of a system [9]. These equations, coupled with equations describing conservation of energy, conservation of mass, and an equation of state (typically the ideal gas law) are used to de-

scribe the flow of a fluid. The first assumption to simplify the Navier-Stokes equations is that the fluid is incompressible. The Navier-Stokes equations in vector form becomes,

$$\rho \frac{D\boldsymbol{V}}{Dt} = \rho \boldsymbol{g} - \boldsymbol{\nabla} p + \mu \boldsymbol{\nabla}^2 \boldsymbol{V} \tag{44}$$

where, ρ is the density of the fluid, $D\boldsymbol{V}/Dt$ is the material derivative of the velocity vector of the fluid, $\boldsymbol{g}$ is the vector acceleration of gravity, and μ is the viscosity [16]. Another equation that is useful to define when discussing the Navier-Stokes equations is the continuity equation, which derives from the conservation of mass,

$$\frac{D\rho}{Dt} = -\rho \nabla \cdot \boldsymbol{V} \tag{45}$$

Since we have assumed incompressible flow, the left-hand side of Equation (45) is zero. Another assumption that simplifies the Navier-Stokes equations is that the flow is inviscid. In this case, one obtains Euler's equation,

$$\rho \frac{D\boldsymbol{V}}{Dt} = \rho \boldsymbol{g} - \nabla p \tag{46}$$

If, in addition, the flow is irrotational, then

$$\nabla \times \boldsymbol{V} = 0 \tag{47}$$

Using Equation (45) and (47), one finds the flow is completely described by Laplace's equation,

$$\nabla^2 \phi = 0 \tag{48}$$

where ϕ represents the velocity fluid flow potential. The assumptions to simplify the Navier-Stokes equations that are implemented by USAERO are that the majority of the flow is

regarded as inviscid, irrotational, and incompressible [1]. Thus, USAERO simplifies the Navier-Stokes equations down to Laplace's equation, shown in Equation (48). USAERO examines objects in an infinite, unbounded environment, so the velocity potential points of interest will be on the wetted surface of the configuration defined in USAERO. Applying Green's Theorem to Laplace's equation for the velocity potential at a point on the wetted surface reveals several integrals which contain the contribution from a surface distribution of normal doublets of strength, a surface distribution of sources of strength, and a wake doublet distribution of strength (in this research, all wake effects were ignored). The doublet distribution on the surface of a configuration is unknown, whereas the source distribution can be determined by the Neumann boundary conditions specifying the normal velocity at the boundary [1].

By solving for the doublets and sources of strength at each time step, the surface velocities and pressure can be evaluated. The flow velocity relative to the surface is comprised of the perturbation velocity, the infinite flow velocity (which is zero in all thesis research case studies), the velocity of the body measured relative to an inertial frame, and the component accounting for any rotational velocity of the body.

The pressure coefficient at each panel center can then be determined using Bernoulli's equation by using a time-stepping approach knowing the velocity of a surface point, V_S, velocity of the configuration, V, and the flow solution at any previous time-step, $\frac{\partial \phi}{\partial t}$ [1].

$$C_p = V_S^2 - V^2 + 2(\frac{\partial \phi}{\partial t}) \tag{49}$$

The forces and moments on each panel on the configuration can then be determined by integrating this pressure coefficient over the wetted surface[1]. In USAERO, the pressure is assumed to be uniform over each panel. This makes defining the panels on a configuration crucial to the accuracy of the results, which will be discussed in Section 3.3. The integration process to determine the forces and moments is therefore reduced to a summation over all

[1] "Wetted surface" refers to the areas on the configuration/body which will be exposed to the flow

of the wetted panels on the configuration.

The force and moments are calculated in USAERO as follows [1]:

$$\vec{C_F} = -\iint_S (C_P\vec{n} - C_f\vec{V}|\vec{V}|)(\frac{dS}{SREF}) \tag{50}$$

and

$$\vec{C_M} = \iint_S \frac{(C_P\vec{n} - C_f\vec{V}|\vec{V}|) \times \vec{R}dS}{SREF \cdot L} \tag{51}$$

where $\vec{n}$ is the outward normal from the surface, C_f is the skin friction contribution (only active if the boundary layer calculation is active - for this research it was turned off), $\vec{V}$ is the flow velocity relative to the surface, SREF is the reference area, $\vec{R}$ is the position vector from a surface point relative to the rotational axis, and L is a reference length (usually mean-chord for pitching moment and semi-span for rolling and yawing moment).

With these force and moment coefficient vectors, we can accelerate the body in USAERO, generate the coefficient vectors, calculate the actual forces and moments using dynamic pressure, and finally graph the results for multiple acceleration cases as discussed earlier.

3.3 Grid Generation and Panel Study

USAERO requires the user to define the geometry of the vehicle under review by generating card sections involving the points and number of panels to be used. However, the question arises, what grid generation pattern is best and how many panels should be defined over each patch[2]? One means to knowing this answer is experience. Experience using the CFD program and knowledge of expected results for flow over bodies would allow the creator to generate a working solution to applying a grid of panels over a body. A more quantitative

[2]A patch is a collection of panels in a rectangular array

means for understanding comes from performing a panel study and calculating/mapping the changes that result with different types of gridding patterns.

3.3.1 Surface Generation

A body can be defined in USAERO's geometry-definition section several different ways. One difficult way, which requires a great understanding of USAERO, would be for the user to create and alter data points directly in the input file. This approach requires a good deal of experience in using and manipulating the code. One user-friendly program which can also be used to generate the geometry is Surfgen. Surfgen is a sister tool to the USAERO CFD package. Surfgen allows the user to create lines, curves, and surfaces from scratch, or enter pre-existing lines and curves from other 3D modeling programs through a shared file format known as the Initial Graphics Exchange Specification (IGES) file. After creating a database of lines and curves in Surfgen, the user can begin to develop connectors over the line which essentially determine the number and location of the panels defined over the body. With Surfgen, several different grids can be generated in order to determine the effects of varying panels on a body. Figure 7 represents an example of generating panels on a body to be analyzed in USAERO. Figure 7 represents a fairly complex model. Surfgen has the ability to create computational grids for these complex figures.

3.3.2 Panel Study

With a given shape and grid pattern defined in USAERO, it is difficult to verify whether or not the flow will be accurately modeled. A panel study provides confidence that the object under review is accurately represented in the flow compared to what would be experienced in a true experimental study. Choosing the number of panels requires some consideration. If too few panels are chosen, the panels across the body will not be able to accurately reflect everything that is occurring within the flow. At the same time, there is a run time limit on the maximum number of panels; the optimal number and configuration of panels is that

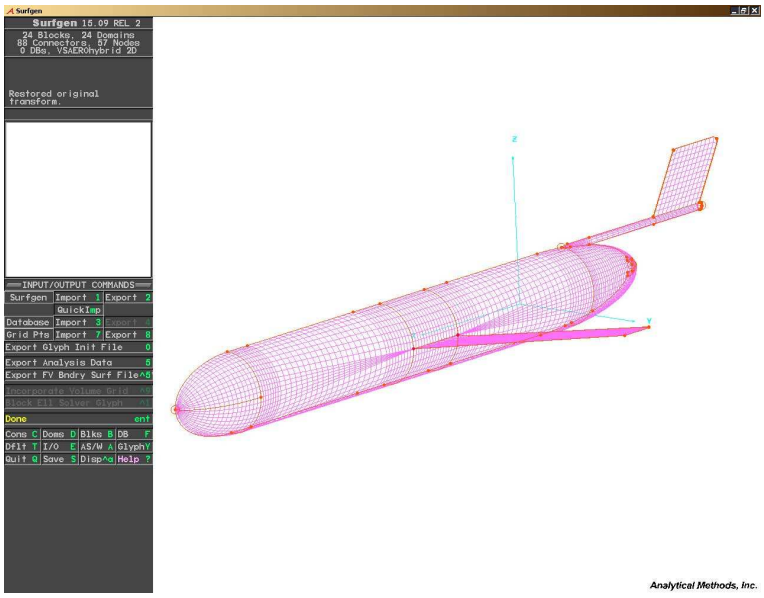

Figure 7: *Slocum* glider in the grid generating program, Surfgen

which provides the necessary accuracy with the minimum computational effort.

Sphere Panel Study

The first simple object which is analyzed in the panel study is the sphere. A sphere is useful since the added mass terms for a submerged sphere are known analytically to be $-\frac{1}{2}m$ as discussed in Section 3.4.1. USAERO can then be used to come up with experimental results to compare to the theoretical results. This procedure can be done several times for a sphere with varying panel density.

Three general locations for determining the pressure coefficient over a sphere are the focus of this study. The three locations are the nose tip (assumed to be the furthest point outward from the body in the x-direction), the midbody location, and a quarter-body location halfway between the leading edge and the midbody location.

As one increases the number of panels, one should expect the pressure coefficient estimated at the nose tip to converge to one. Further, the deviation in pressure coefficient results using

Table 2: Coefficient of Pressure Distribution Based on Panels

No. Panels	Leading Edge	Midbody Location	Quarter-body Location
10	0.939	-1.165	-0.141
14	0.969	-1.201	-0.133
16	0.976	-1.209	-0.351
18	0.981	-1.227	-0.514
20	0.984	-1.232	-0.307
22	0.987	-1.235	-0.446
24	0.989	-1.238	-0.277
26	0.991	-1.239	-0.398
28	0.992	-1.241	-0.499
30	0.993	-1.243	-0.363
40	0.996	-1.246	-0.391
50	0.997	-1.248	-0.408
60	0.998	-1.249	-0.418

different panel resolutions decreases as the number of panels increases. The data listed in Table 2 can be displayed visually. Figure 8 shows a progression of results for a sphere in USAERO using increasingly high panel resolutions.

Starting from the upper left, moving to the right, the panels displayed in Figure 8 have 10, 20, 30, 40, 50, and 60 panels, respectively. The flow is more accurately represented by using higher panel resolutions.

One way to interpret the results listed in Table 2 is to graph an error function as the number of panels increases. In an inviscid solution, the pressure coefficient at the beginning or tip of an object in a flow should have a pressure coefficient equal to 1.0. An error function can be determined based on the results obtained from each panel study after analyzing the nose tip location. Essentially, this study is looking for a general answer as to how many panels are "enough" over a prescribed geometry in order to accurately capture the flow effects. Another

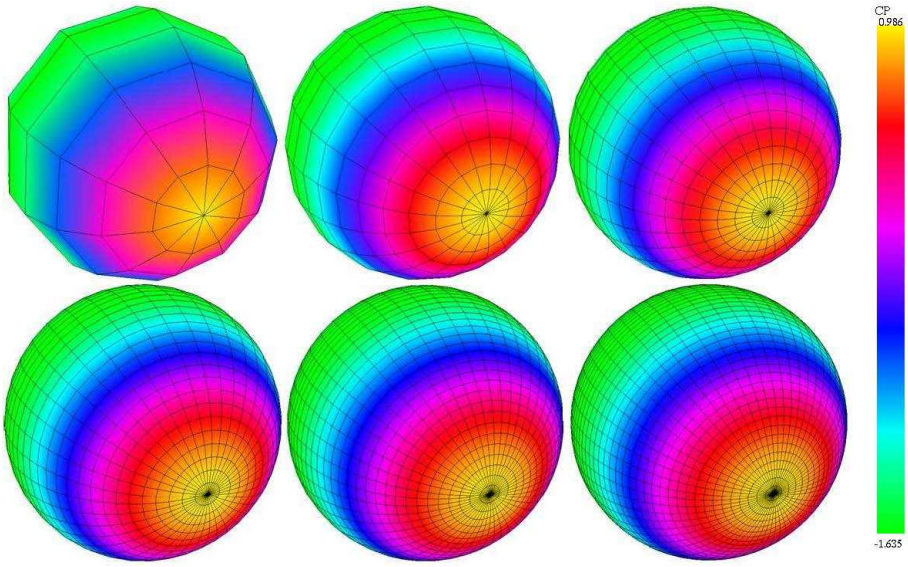

Figure 8: Panel Progression

way to consider it is: for a given increase in panels, is there a significant increase in accuracy of the results. This rationale suggests finding a bend or a knee on a graph.

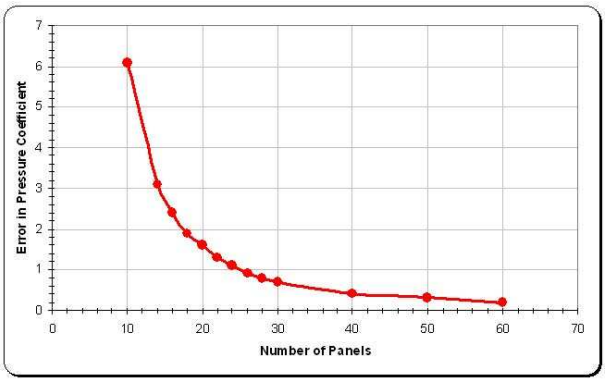

Figure 9: Pressure Coefficient Error with respect to No. Panels

From Figure 9 it can be seen that, at around 26 panels defined on the body, there is roughly 1 percent error between the theoretical value of pressure coefficient and the computed value. This point also corresponds to the bend or knee in the graph and thus may be deemed an appropriate number of panels for a sphere.

Another method that could be used to compare the effect of increasing the number of panels

is to compare the added mass terms of the sphere for each panel study. In theory, as we increase the number of panels, the computed value of added mass should approach the theoretical value. The equations for determining added mass of a sphere are developed in Section 3.4.1.

In this example, $\rho = 1.9905$ slugs/ft^3 and the radius of the sphere is 6 ft. This corresponds to an actual added mass of 900.48 slugs. For the panel cases described above, the added mass can be calculated and compared to this theoretical value of added mass. The percent error is determined by the following,

$$PercentError = \frac{|Actual - Experimental|}{Actual}(100) \tag{52}$$

where the terms *Actual* and *Experimental* refer to the known and computed results, respectively, for the added mass of a sphere.

Table 3: Added Mass Comparison for Panel Study of a sphere

No. Panels	$X_{\dot{u}}[slugs]$	Percent Error
10	818.7	9.08
16	868.9	3.51
20	880.7	2.20
24	886.9	1.51
30	892.2	0.92
40	896.2	0.48

Again, as expected, increasing the number of panels on the body does decrease the error between theoretical and experimental results. In Table 3, there is a 1 percent error around 24 to 26 panels defined on the body. Again, however, this is a sphere which is a very simple shape to analyze. Figure 10 gives another representation of the data presented in Table 3.

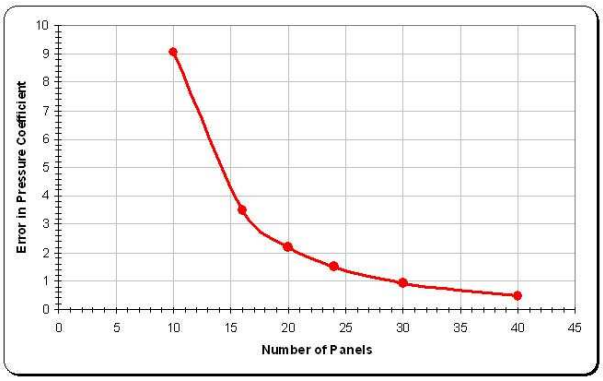

Figure 10: Added Mass Error with respect to No. Panels

Complex Shape Panel Study

In most models, there are several different sections of varying curvature and complexity. Consider the model shown in Figure 11, a model of the Virginia Tech Miniature Autonomous Underwater Vehicle (VTMAUV) created in Rhinoceros 3.0.

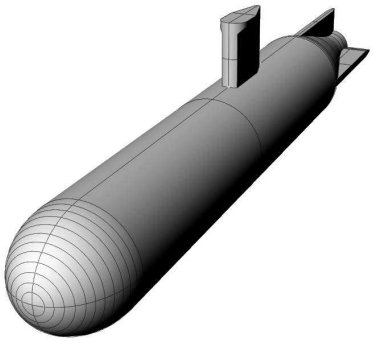

Figure 11: 475 VTMAUV in Rhinoceros 3.0

This model has not previously been analyzed in a CFD program, thus it is difficult to know how many panels to define at any location on the body in order to generate an accurate model in the CFD program. A similar panel study like the one on the sphere can be performed to obtain a solution. For this more complex shape, however, the panel density will not be

uniform over the body. For example, it would be wise to assume that more panels should be generated around the nose section since there is more curvature there, but how many panels are enough? The same question arises for the mid-body section where there is no curvature, as well as the tail section and the section between the tail fins. To answer these questions, a convergence study is performed on the 475 VTMAUV in which a series of case studies are analyzed. Each case study has a different number of panels defined at the different locations on the 475 VTMAUV. In theory, as the number of panels is increased in a region of a given panel, there should be a smaller change in the pressure coefficient at the panel under review, suggesting convergence.

In this complex panel study, nine areas on the 475 VTMAUV are chosen for analysis: the nose, a nose/body location, a body location, a pre-mast body location, an aft-mast body location, the front (leading edge) of the mast, a body/tail location, a mid-tail location, and a tail/end location. In each of these areas the number of panels defined is altered as shown in Table 4.

Table 4: Number of Panels Defined per Study

Case	Nose	Nose/Body	PMB	LE Mast	AMB	Body/Aft	Mid-Tail	Aft/End
1	5	2	6	6	3	2	4	2
2	7	3	8	8	5	3	6	3
3	9	4	10	10	7	4	8	4
4	11	5	12	12	9	5	10	5
5	13	6	14	14	11	6	12	6
*6	14	7	16	16	13	7	14	7
7	17	8	18	18	15	8	16	8
*8	19	9	20	20	16	10	18	9
9	21	10	22	22	17	12	20	10
*10	23	11	24	24	18	14	22	11

Here, “PMB” refers to the pre-mast body location and “AMB” refers to the aft-mast body

location. In the early cases, some panels have very high aspect ratios and are definitely not the proper number required to accurately model the sections. However, they were only meant to aid in convergence to a solution. In the same manner, the last panel study had a tremendously large number of panels defined on the entire body, more than necessary over relatively simple sections such as the mid-body.

In each of the ten case studies that were performed, the pressure coefficient values at the locations described above were determined. Table 5 shows the panel study analysis for the seven case studies at the various locations along the body.

Table 5: Pressure Coefficient Distribution over Panels based on Case No.

Case	Nose	MN	Nose/Body	PM	LEM	AM	Body/Aft	Mid-Tail	End
1	0.883	-0.389	-0.217	-0.0155	0.419	-0.0273	-0.174	0.0774	0.427
2	0.944	-0.341	-0.257	-0.0159	0.705	0.0079	-0.229	0.0778	0.592
3	0.967	-0.305	-0.272	-0.0176	0.856	-0.0045	-0.297	0.0706	0.630
4	0.977	-0.288	-0.284	-0.0178	0.912	-0.0019	-0.338	0.0693	0.642
5	0.982	-0.273	-0.292	-0.0177	0.918	-0.0001	-0.372	0.0684	0.646
*6	0.984	-0.260	-0.299	-0.0173	0.936	0.0064	-0.378	0.0686	0.645
7	0.986	-0.383	-0.304	-0.0172	0.939	0.0075	-0.399	0.0683	0.646
*8	0.987	-0.366	-0.312	-0.0171	0.939	0.0057	-0.421	0.0681	0.646
9	0.988	-0.333	-0.315	-0.0172	0.952	0.01	-0.453	0.0684	0.646
*10	0.989	-0.359	-0.313	-0.017	0.954	0.0072	-0.447	0.0685	0.646

Here, “MN” refers to mid-nose location, “PM” refers to pre-mast location, “LEM” refers to the leading edge location on the mast, and “AM” refers to aft mast location. In Tables 4 and 5 the * refers to a step in the file creation process where additional panels had to be defined in the y-z direction, as opposed to only changing panel density in the x-direction. This was done in order to avoid the panels becoming too large in one direction and having too high of an aspect ratio, which leads to poor analysis. Looking at Table 5, it can be seen that there is some convergence of the values at certain locations. Since there are no

known data values to measure against, there is no way of knowing how many panels are sufficient. One way to be sure of a solution for a study like this is to graph the results of each case study and compare the difference between results. As the case studies increase in panel density, the change will be less each time and finally the change will be negligible. This convergence solution is one way to obtain the proper number of panels to define over a given body location. For each of the AUV's analyzed in this thesis that are created from Surfgen, this technique is used. Figure 12 represents the tables above in graphical form, which should make it more clear how a final solution is obtained.

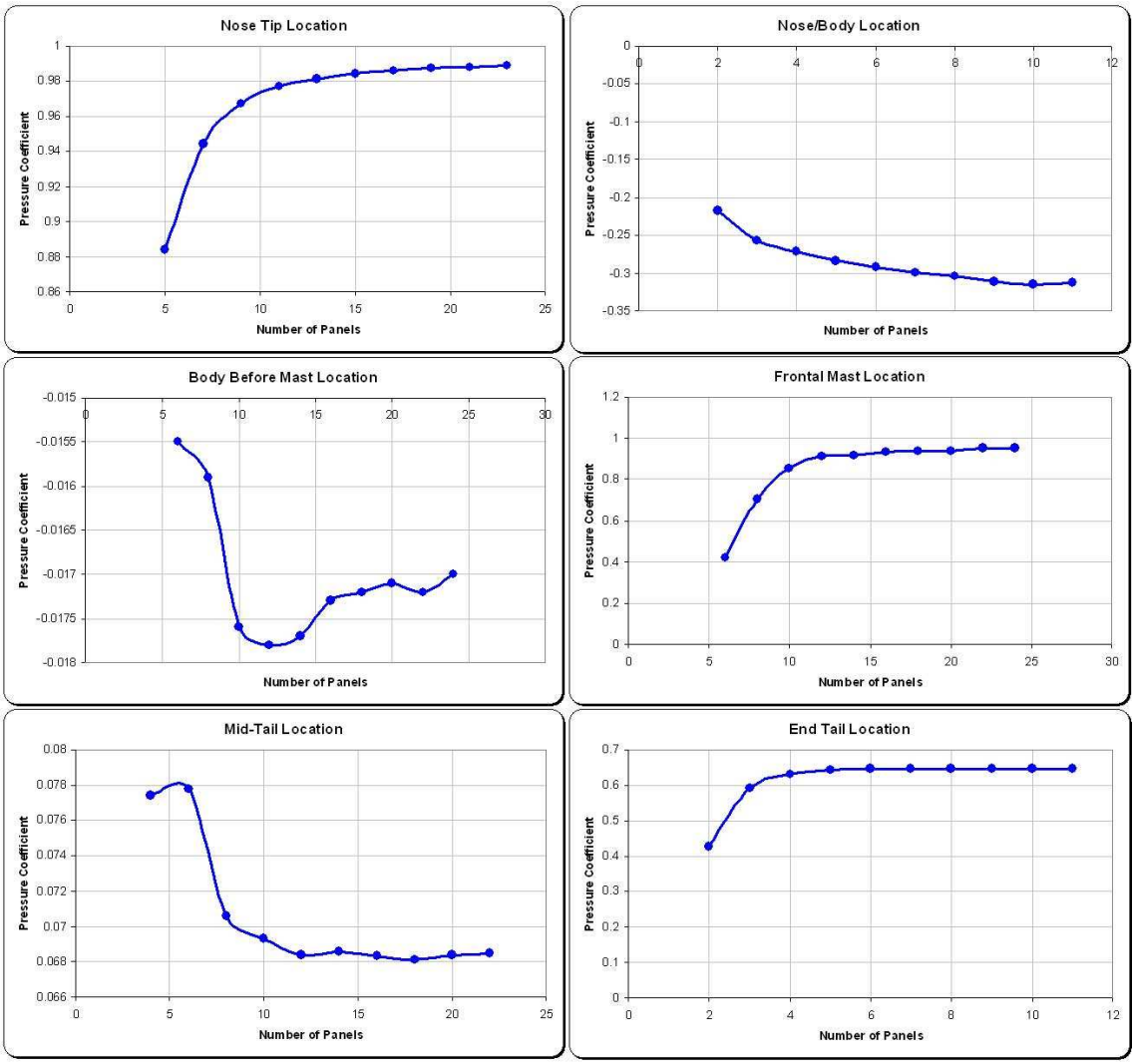

Figure 12: VTMAUV Panel Study

Figure 12 does not show all of the panel locations graphed since some sections under analysis (i.e. Mid-Nose) are under the same panel density as other sections (i.e. Nose). In order to determine the final solution on the number of panels, one could go through graph by graph and make a decision where the increase in panels no longer yields a much more accurate result. Looking at the "Nose Tip Location" graph indicates that around 20 panels defined on the nose, the pressure distribution isn't varying greatly. Other sections such as the "Body Before Mast Location" graph may seem difficult to decide on the proper number of panels. However, looking at the pressure coefficients on the y-axis reveals that the panels from case to case are only changing by 0.0001 after 15 panels or more are defined on the location. This same method can be carried out for all locations. Thus, a final solution to the panel distribution on the model can be represented below as shown in Table 6

Nose	Nose/Body	Pre-Mast	LE Mast	Aft-Mast	Aft/Tail	Mid-Tail	End
21	10	16	20	13	10	14	5

Table 6: Final Panel Study Distribution

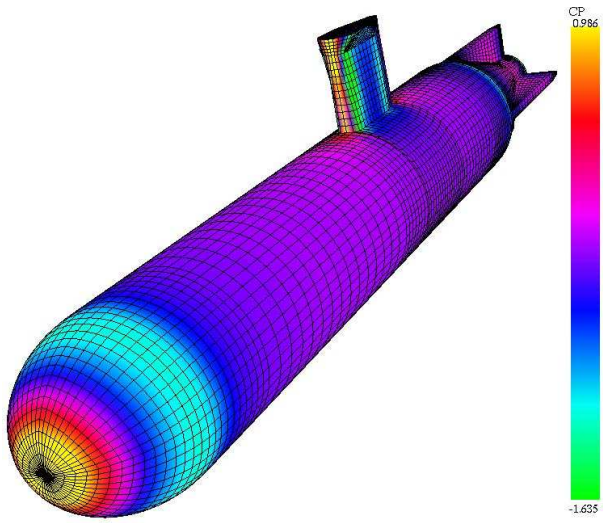

Figure 13: Final Panel Result for VTMAUV Study

3.4 Validation of the Approach

In order to validate the approach, added inertia matrices for two geometries with analytical solutions were determined. This process serves two tasks. The first task is to determine the accuracy and validity of USAERO compared to known computational results. The second task is to gain further understanding of how the program works by setting up and running multiple simulations and debugging the process. Two cases were analyzed for simple bodies of revolution; a sphere and a spheroid. These two objects were chosen because one may compare computational solutions to known solutions for added mass/inertia.

3.4.1 Sphere

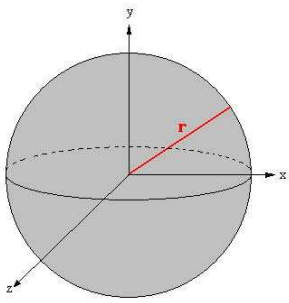

Figure 14: Sphere with radius r

Consider a sphere as shown in Figure 14 with a radius of 3 ft and a density of 1.9905 slug/ft^3 (the density of seawater). The added mass of a sphere is known to be:

$$X_{\dot{u}} = Y_{\dot{v}} = Z_{\dot{w}} = -(1/2)m \tag{53}$$

where m is the mass of the displaced fluid:

$$m = \rho(4/3)\pi r^3 \tag{54}$$

Therefore,

$$X_{\dot{u}} = Y_{\dot{v}} = Z_{\dot{w}} = -\frac{2}{3}\rho\pi r^3 \tag{55}$$

Also, because of spherical symmetry

$$L_{\dot{p}} = M_{\dot{q}} = N_{\dot{r}} = 0 \tag{56}$$

From these equations it can be determined that for a sphere of radius = 3ft and density = 1.9905 slugs per cubic ft, the added mass terms should yield $X_{\dot{u}}$ = -112.56 slugs and the added mass/inertia matrix is represented by Equation (57).

$$\boldsymbol{M_A} = -\begin{bmatrix} 112.56 & 0.0000 & 0.0000 & 0.0000 & 0.0000 & 0.0000 \\ 0.0000 & 112.56 & 0.0000 & 0.0000 & 0.0000 & 0.0000 \\ 0.0000 & 0.0000 & 112.56 & 0.0000 & 0.0000 & 0.0000 \\ 0.0000 & 0.0000 & 0.0000 & 0.0000 & 0.0000 & 0.0000 \\ 0.0000 & 0.0000 & 0.0000 & 0.0000 & 0.0000 & 0.0000 \\ 0.0000 & 0.0000 & 0.0000 & 0.0000 & 0.0000 & 0.0000 \end{bmatrix} \tag{57}$$

Using the same given inputs in USAERO as mentioned above, analysis can be performed on the sphere and its added mass/inertia matrix can be computed.

$$\boldsymbol{M_A} = -\begin{bmatrix} 112.07 & 0.0000 & 0.0000 & 0.0000 & 0.0000 & 0.0000 \\ 0.0000 & 112.43 & 0.0000 & 0.0000 & 0.0000 & 0.0000 \\ 0.0000 & 0.0000 & 112.43 & 0.0000 & 0.0000 & 0.0000 \\ 0.0000 & 0.0000 & 0.0000 & 0.0000 & 0.0000 & 0.0000 \\ 0.0000 & 0.0000 & 0.0000 & 0.0000 & 0.0000 & 0.0000 \\ 0.0000 & 0.0000 & 0.0000 & 0.0000 & 0.0000 & 0.0000 \end{bmatrix} \tag{58}$$

The difference between theoretical values and USAERO calculated values is seen to be extremely small. In order to improve accuracy, more panels could be gridded on the body, as

will be described in Section 3.3.2.

3.4.2 Spheroid

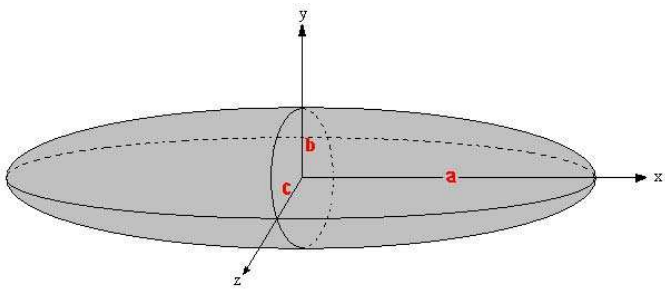

Figure 15: Ellipsoid with semi-axes a, b, and c [6]

The next validation case considers a slightly more complicated object, a spheroid. The same process described in Section 6 is performed. Using Figure 15 and setting a=10 ft, b = 5 ft, and c = 5 ft along with the same density of seawater, a test case can be performed on this prolate spheroid to determine the added mass/inertia terms. This case is relevant since additional added inertia terms should show up in the solution, unlike the sphere case. For a prolate spheroid, the eccentricity is defined as [6]:

$$e = \sqrt{1 - (b/a)^2} \tag{59}$$

Other parameters are,

$$\alpha_0 = \frac{2(1-e^2)}{e^3}(\frac{1}{2}\ln\frac{1+e}{1-e} - e) \tag{60}$$

$$\beta_0 = \frac{1}{e^2} - \frac{1-e^2}{2e^3}\ln\frac{1+e}{1-e} \tag{61}$$

where the mass of the prolate spheroid is:

$$m = \frac{4}{3}\pi\rho a b^2 \tag{62}$$

With these definitions,

$$X_{\dot{u}} = -\frac{\alpha_0}{2-\alpha_0}m \tag{63}$$

$$Y_{\dot{v}} = Z_{\dot{w}} = -\frac{\beta_0}{2-\beta_0}m \tag{64}$$

$$L_{\dot{p}} = 0 \tag{65}$$

$$N_{\dot{r}} = M_{\dot{q}} = -\frac{1}{5}\frac{(b^2-a^2)^2(\alpha_0-\beta_0)}{2(b^2-a^2)+(b^2+a^2)(\beta_0-\alpha_0)}m \tag{66}$$

Using Equations (63 - 66) gives the added mass/inertia solution, in English units, for the given prolate spheroid, presented in Equation (67).

$$\boldsymbol{M_A} = -\begin{bmatrix} 437.77 & 0.00 & 0.00 & 0.00 & 0.00 & 0.00 \\ 0.00 & 1467.89 & 0.00 & 0.00 & 0.00 & 0.00 \\ 0.00 & 0.00 & 1467.89 & 0.00 & 0.00 & 0.00 \\ 0.00 & 0.00 & 0.00 & 0.00 & 0.00 & 0.00 \\ 0.00 & 0.00 & 0.00 & 0.00 & 12476.66 & 0.00 \\ 0.00 & 0.00 & 0.00 & 0.00 & 0.00 & 12476.66 \end{bmatrix} \tag{67}$$

The same approach for validation of the sphere is used to validate the spheroid. Multiple accelerations in each of the degrees of freedom are performed to determine the coefficients of force and moment. Equation (68) shows the added mass/inertia matrix generated using USAERO.

$$\boldsymbol{M_A} = -\begin{bmatrix} 435.22 & 0.00 & 0.00 & 0.00 & 0.00 & 0.00 \\ 0.00 & 1467.5 & 0.00 & 0.00 & 0.00 & 0.00 \\ 0.00 & 0.00 & 1465.6 & 0.00 & 0.00 & 0.00 \\ 0.00 & 0.00 & 0.00 & 0.02 & 0.00 & 0.00 \\ 0.00 & 0.00 & 0.00 & 0.00 & 12691 & 0.00 \\ 0.00 & 0.00 & 0.00 & 0.00 & 0.00 & 12719 \end{bmatrix} \tag{68}$$

Comparing Equations (67) and (68) shows that the added mass matrix from USAERO closely resembles the predicted values from theory. Again, in order to get more accuracy, more panels could be used in USAERO as described in Section 3.3.2.

3.5 Gliders

One of the primary focuses of this thesis is to determine the added mass/inertia of current underwater gliders. The following two sections describe two specific gliders that are considered here.

From Section 2, it has been shown that a solution of the added mass/inertia matrix should hold the form shown in Equation (69), assuming that the model under review has two or more planes of symmetry [10]. This is the general solution for a added mass/inertia matrix for a body with two planes of symmetry.

$$\boldsymbol{M_A} = -\begin{bmatrix} X_{\dot{u}} & 0 & 0 & 0 & 0 & 0 \\ 0 & Y_{\dot{v}} & 0 & 0 & 0 & Y_{\dot{r}} \\ 0 & 0 & Z_{\dot{w}} & 0 & Z_{\dot{q}} & 0 \\ 0 & 0 & 0 & L_{\dot{p}} & 0 & 0 \\ 0 & 0 & M_{\dot{w}} & 0 & M_{\dot{q}} & 0 \\ 0 & N_{\dot{v}} & 0 & 0 & 0 & N_{\dot{r}} \end{bmatrix} \tag{69}$$

3.5.1 *Slocum*

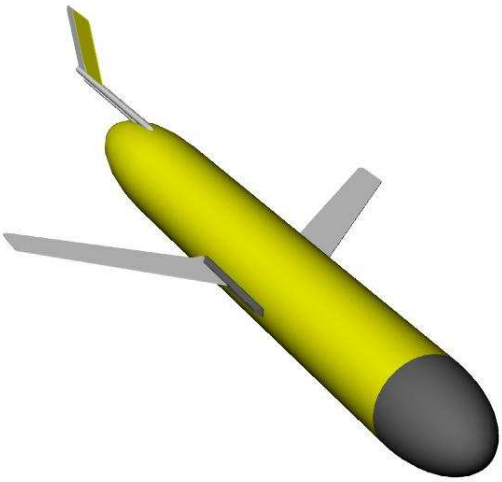

Figure 16: *Slocum* glider in Rhinoceros 3.0

The *Slocum* glider, described in Section 1.1, is a more conventional glider which has been the focus of several analytical and experimental studies [2, 7]. Unfortunately, none of these studies has included proper estimates of the added mass and inertia terms. To provide some sound basis for evaluating theoretical results, as applied to the *Slocum* vehicle, the generalized added inertia matrix for this vehicle has been obtained. The *Slocum* model first began in Rhinoceros 3.0, as shown in Figure 16, and was broken down into components. These components were then transferred into Surfgen, described in Section 3.3.1. From there, a grid generated model was produced for the vessel after an extensive panel study was performed, which is detailed in Appendix B.1. A representation of *Slocum* in USAERO can be seen in Figure 17.

The body frame is fixed in the conventional way, with the x-axis pointing towards the nose and the z-axis downward through the belly. The origin of this frame is the center of buoyancy (center of volume) location of the displaced fluid determined from Rhinoceros 3.0 (i.e. the volume centroid of the model). The center of buoyancy of *Slocum* is located at (-2.878, 0, 0.0019) feet measured from the nose tip of the vehicle.

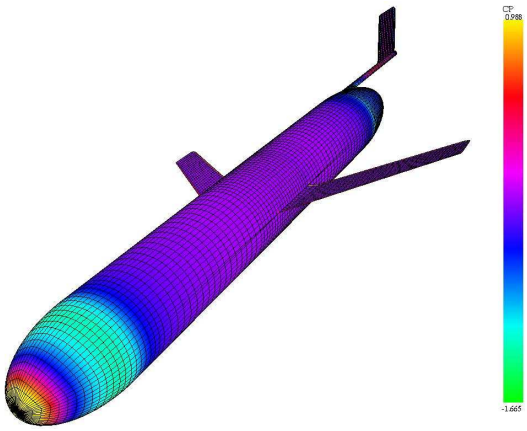

Figure 17: *Slocum* glider in USAERO

Equation (70) provides the final result of the generalized added inertia matrix for the *Slocum* glider, where all quantities are provided in English units (slugs, slug-feet, and slug-feet^2, respectively), as obtained by the USAERO methods described previously. Section B.1 provides an in-depth analysis on the panel study used for *Slocum*.

$$\left[\begin{array}{c|c} \boldsymbol{M}_{\mathbf{f}} & \boldsymbol{C}_{\mathbf{f}}{}^{T} \\ \hline \boldsymbol{C}_{\mathbf{f}} & \boldsymbol{I}_{\mathbf{f}} \end{array}\right]_{\text{Slocum}} = \begin{bmatrix} -0.159 & 0.000 & 0.000 & 0.000 & 0.000 & 0.000 \\ 0.000 & -3.946 & 0.000 & 0.125 & 0.000 & 0.798 \\ 0.000 & 0.000 & -4.562 & 0.000 & -0.344 & 0.000 \\ 0.000 & 0.125 & 0.000 & -0.566 & 0.000 & -0.438 \\ 0.000 & 0.000 & -0.355 & 0.000 & -7.80 & 0.000 \\ 0.000 & 0.799 & 0.000 & -0.438 & 0.000 & -10.49 \end{bmatrix} \tag{70}$$

Comparing Equation (70) to Equation (69) shows four additional terms. These terms show up for the *Slocum* glider due to the asymmetry of the vehicle; *Slocum* has only one plane of symmetry, the longitudinal plane. A graphical solution to how we obtained the values in Equation (70) is presented in Figures 18 and 19. For each degree of freedom in acceleration, the respective forces and moments are shown.

A further parameters that can be estimated is the inertia of the rigid body, $\boldsymbol{I}_{\mathbf{rb}}$. This

calculation is made from the completed model in Rhinoceros 3.0. As described previously, Rhinoceros 3.0 treats the vehicle as a body of uniform mass/volume and calculates the centroid of that uniform volume. The units from Rhinoceros 3.0's calculation is in ft^5. If we multiply this matrix by the density of the fluid which the vehicle will be in, then we can get like-terms for the rigid body inertia and the added inertia calculated from USAERO. The units of Equation (71) are in slugs·ft^2.

$$\boldsymbol{I}_{\mathbf{rb}} = \begin{bmatrix} 0.251 & 0 & 0 \\ 0 & 9.719 & 0 \\ 0 & 0 & 9.719 \end{bmatrix} \tag{71}$$

3.5.2 *XRay/Liberdade*

The *XRay* glider is a blended wing-body autonomous underwater vehicle [8]. As for many AUVs, the added mass and inertia terms are unknown and are difficult and costly to measure through experiments. The representation of the *XRay* glider was obtained from the 3-D modeling program, Rhinoceros 3.0, after importing geometry provided by collaborators at the SIO/MPL. Rhinoceros 3.0 was used to help create the point files, which were then used to create the patch data section of the input file for the *XRay* in USAERO, as shown in Figure 20 in the manner described in Section 3.3.1.

With the model geometry properly incorporated, the added mass/inertia matrix can be computed. The body frame is fixed in the non-conventional way, with the x-axis pointing towards the nose and the z-axis upward through the belly. The origin of this frame is located at the center of volume of the body, which was determined from Rhinoceros[3]. The center of volume is located at (-3.814, 0, 0.004) feet from the nose tip of the vehicle. To appreciate the scale, note that the length along the centerline from the nose-tip to tip of the tail along

[3]Rhinoceros 3.0 calculates the volume centroid of all closed polysurfaces selected. It treats each volume's mass as uniformly distributed.

the centerline is 7.309 feet.

The panel study done on the vehicle can be seen in Section C.1. Equation (72) provides the finalized results of the generalized added inertia matrix for the *XRay* glider, where all quantities are provided in English units (slugs, slug-feet, and slug-feet^2).

$$\left[\begin{array}{c|c} \boldsymbol{M_f} & \boldsymbol{C_f}^T \\ \hline \boldsymbol{C_f} & \boldsymbol{I_f} \end{array}\right]_{\text{XRay}} = \begin{bmatrix} -18.32 & 0.00 & 0.00 & 0.00 & 0.00 & 0.00 \\ 0.00 & -10.86 & 0.00 & 4.68 & 0.00 & 29.85 \\ 0.00 & 0.00 & -261.3 & 0.00 & -84.22 & 0.00 \\ 0.00 & 4.52 & 0.00 & -3030.8 & 0.00 & -12.16 \\ 0.00 & 0.00 & -85.81 & 0.00 & -285.1 & 0.00 \\ 0.00 & 28.72 & 0.00 & -14.94 & 0.00 & -300.1 \end{bmatrix} \tag{72}$$

Comparing Equation (72) to Equation (69) reveals four additional terms. These terms show up for the *XRay/Liberdade* glider due to the asymmetry of the vehicle; *XRay/Liberdade* has only one plane of symmetry, the longitudinal plane. In graphical form, the values in Equation (72) are obtained from Figures 21 and 22.

The rigid body inertia matrix can also be computed for the *XRay/Liberdade* glider, as was done for the *Slocum* glider. This is done in Rhinoceros 3.0 by calculating the volume moments of inertia, whose units are in ft^5. Multiplying by the density of the surrounding fluid gives the proper matching units to the added inertia matrix, which are slugs·ft^2.

$$\boldsymbol{I_{rb}} = \begin{bmatrix} 910.2 & 0 & 0 \\ 0 & 131.9 & 0 \\ 0 & 0 & 1030.2 \end{bmatrix} \tag{73}$$

3.5.3 Error in Glider Results

There is some error present in determining the final solutions to the generalized added mass matrices that should be addressed. When analyzing the force and moment coefficient data from USAERO's output, the non-steady terms which are analyzed are chosen at random. The steady terms, such as force in the x-direction due to acceleration in the x-direction, are virtually unchanging throughout the time-steps of the computational flight test and thus it is clear which "value" which should be plotted for the linear curve fit analysis. However, the unsteady terms, such as force in the z-direction due to acceleration in the x-direction, range in value and it becomes difficult to pick the "accurate" term for the linear curve fit analysis. As a result, a non-linear trend or confusing plot may be generated. This is not indicative of a trend or pattern in the data, but instead simply an effect of random selection, which should aid in the visualization that in fact there is no linear trend to that particular data and thus it should be ignored.

Another source of error on the final results for the vehicles studied in this research is to note that through the panel studies, we determined how many panels defined on the body were "enough" to accurately model the flow around the geometry. To get more accurate results, however, would mean that the geometry should be panelled at a much higher resolution. This will increase the run-time of the trials significantly for only a little more accuracy in the results.

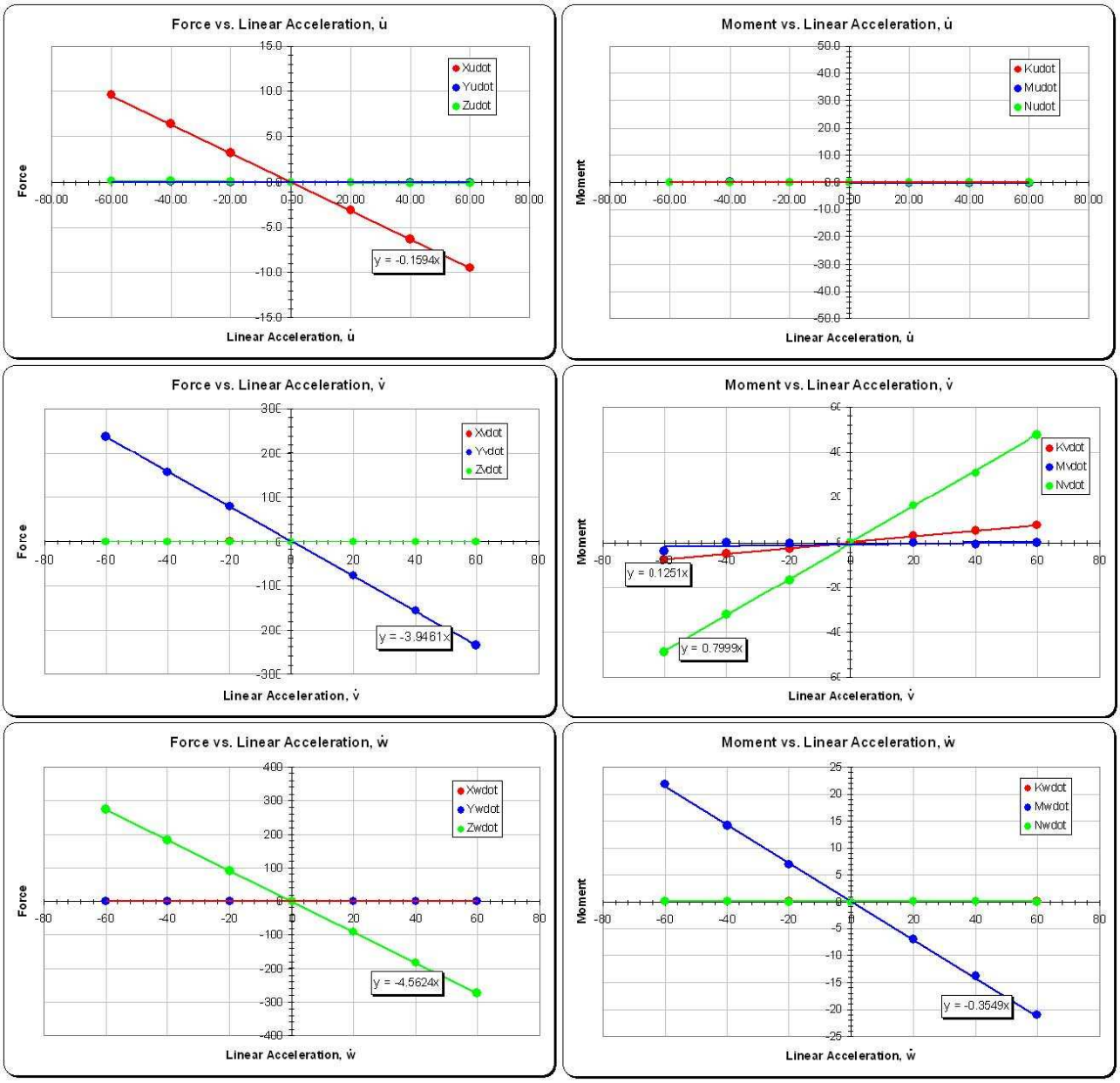

Figure 18: Slocum Added Mass/Inertia due to Linear Accelerations

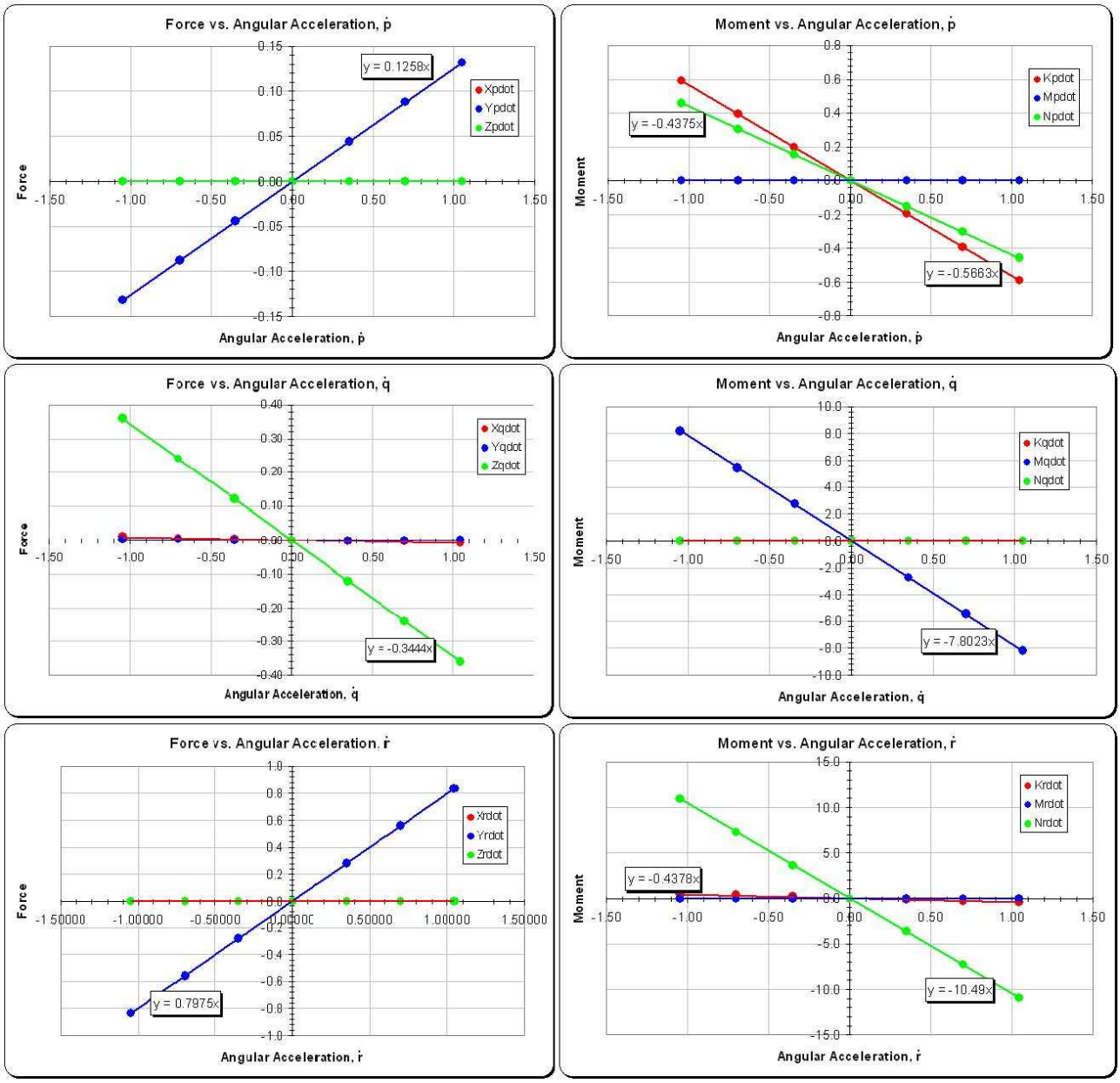

Figure 19: Slocum Added Mass/Inertia due to Angular Accelerations

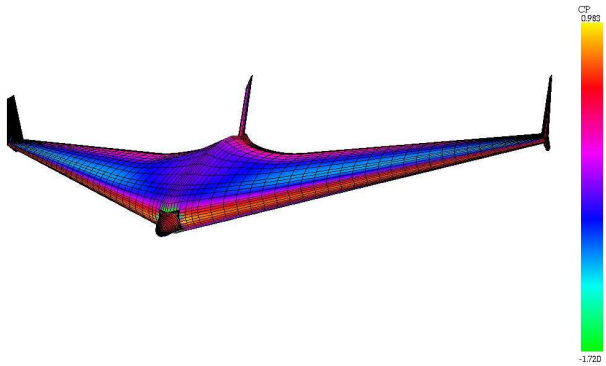

Figure 20: *XRay* Glider in USAERO/OMNI3D

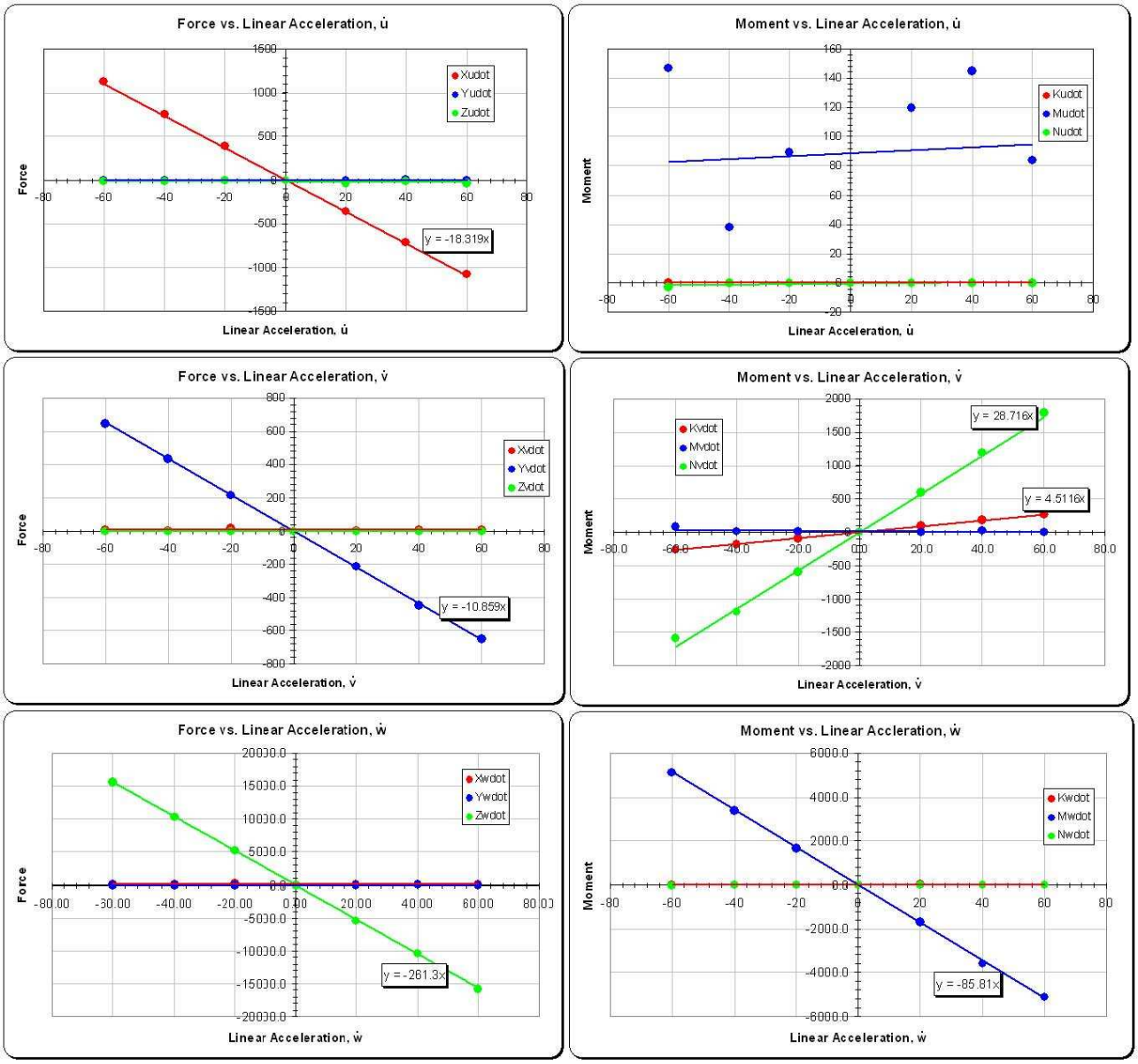

Figure 21: *XRay/Liberdade* Linear Acceleration Terms

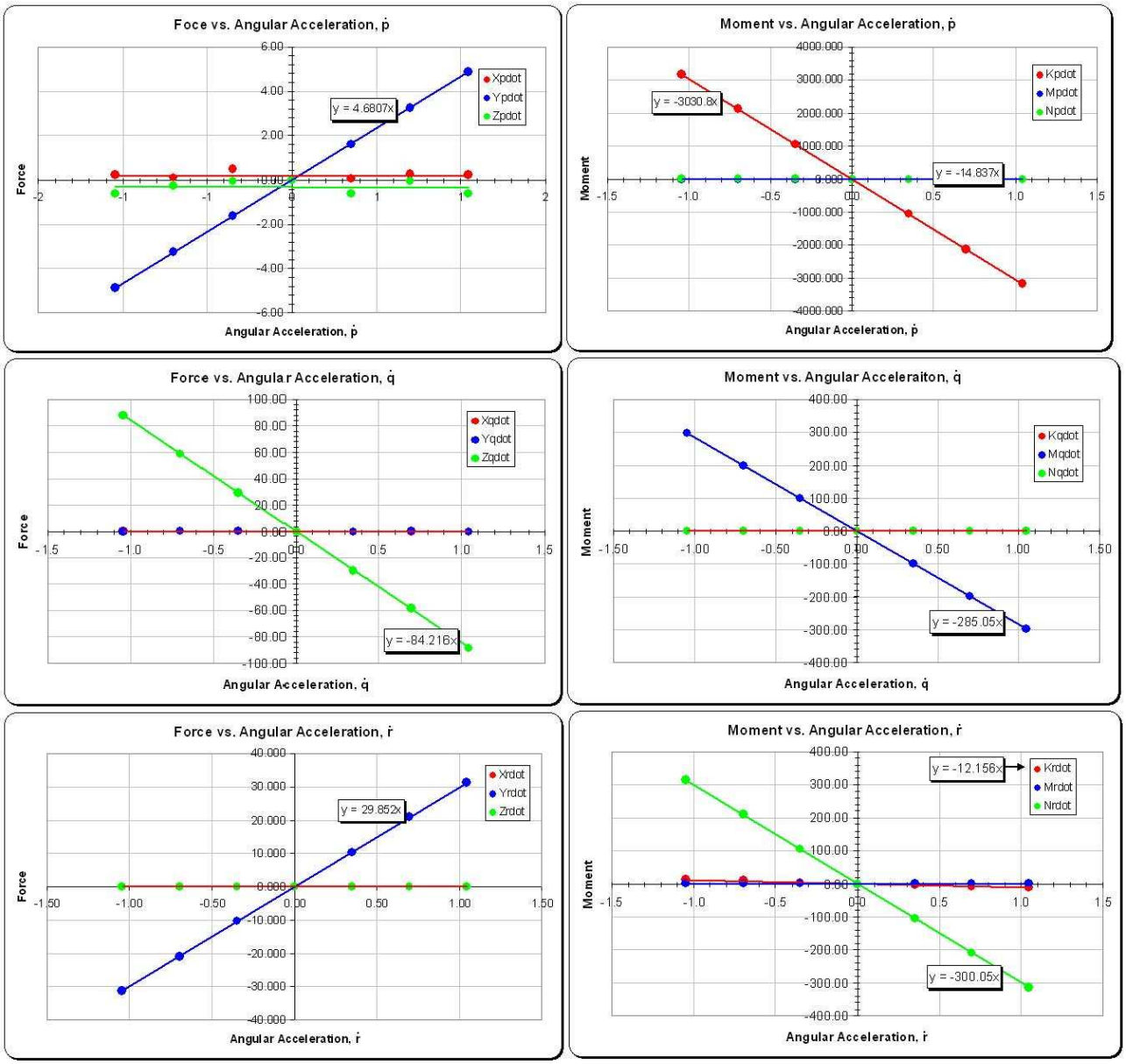

Figure 22: *XRay/Liberdade* Angular Acceleration Terms

4 Viscous Coefficients from Semi-empirical Estimates

Stability coefficients have been determined for the *Slocum* glider using semi-empirical techniques. Table 7 describes these parameters. The method of obtaining these viscous coefficients is described and applied in Appendix A.

A list of parameters describing the model is required. Using Rhinoceros 3.0 and the figures defined in [13], a complete table of geometric parameters was generated. Table 7 shows this table of geometric parameters used to determine the viscous coefficients. Examples of calculations involving these geometric parameters are shown in Appendix A.

Using the parameter values listed in Table 7 and following the outlined approach detailed in [13], the results for the viscous coefficients for *Slocum* are calculated and presented in Table 8.

Name	Symbol	Value
a	Speed of Sound	4921 ft/s
A	Aspect Ratio	7.21
$A_{v_{eff}}$	Effective Aspect Ratio of Tail	0.87
b	Wing Span	3.21 ft
b_v	Tail Span	0.52 ft
$\overline{c}$	Chord length at CG	0.43 ft
c_r	Root Chord	0.52 ft
c_t	Tip Chord	0.37 ft
d_f	Fuselage Diameter	0.69 ft
l_f	Length of Fuselage	5.89 ft
l_v	Horizontal Length of Tail CG from Body CG	4.08 ft
S	Wing Surface Area	1.43 ft^2
S_v	Tail Surface Area	0.31 ft^2
S_{wet_w}	Wing Wetted Surface Area	1.07 ft^2
λ	Taper Ratio	0.69
S_{B_s}	Fuselage Surface Area	3.81 ft^2
m	Mass	50 kg
M	Mach Number	0.0005
n_{ac}	X-Distance Wing CL to AC	1.07 ft
n_{mgc}	X-Distance Wing CL to LE	0.97 ft
V	Speed of Glider	2.54 ft/s
W	Weight of Glider	110.2 lb_f
$\bar{x}_{ref}$	X-Location CG body to CG wing	-0.942

Table 7: List of Knowns for Calculations

Name	Symbol	Value
x_m	X-Location of CG	2.88 ft
z_v	Vertical Height of Tail CG from Body CG	0.61 ft
α	Angle of Attack	4.25^o
z_w	Vertical location of wing w/r to CG	0
$\Lambda_{(c/2)t}$	Half-chord sweep angle of tail	29.8^o
$\Lambda_{(c/4)t}$	Quarter-chord sweep angle of tail	29.8^o
$\Lambda_{(c/2)w}$	Half-chord sweep angle of wing	42.6^o
$\Lambda_{(c/4)w}$	Quarter-chord sweep angle of wing	43.8^o
Γ	Dihedral angle of wing	0°
R_{N_f}	Reynolds Number of fuselage	$0.235\text{x}10^6$
t/c	Thickness-to-chord ratio	0.016
δ_f	Flap Deflection	0°
ε_t	Wing Twist value	0°
C_L	Lift Coefficient due to weight	12.03
$x_{cg(w)}$	Distance from Wing front to CG location on chord at CG	0.22 ft
$x_{ac(w)}$	Distance from Wing front to AC location on chord at CG	0.11 ft

Table 8: Viscous Coefficients for *Slocum*

Symbol	Name	Value [1/rad]
C_{L_α}	Lift-Due-To-Angle-of-Attack	3.73
C_{m_α}	Pitching-Moment-Due-To-Angle-of-Attack	-0.15
C_{l_β}	Rolling-Moment-Due-To-Sideslip	-1.43
C_{n_β}	Yawing-Moment-Due-To-Sideslip	4.85
C_{y_β}	Side-Force-Due-To-Sideslip	-0.32
C_{y_p}	Side-Force-Due-To-Roll-Rate	0.10
C_{l_p}	Roll-Moment-Due-To-Roll-Rate	-0.78
C_{n_p}	Yawing-Moment-Due-To-Roll-Rate	-1.19
C_{m_q}	Pitching-Moment-Due-To-Pitch-Rate	-0.04
C_{y_r}	Side-Force-Due-To-Yaw-Rate	0.45
C_{l_r}	Rolling-Moment-Due-To-Yaw-Rate	1.62
C_{n_r}	Yawing-Moment-Due-To-Yaw-Rate	-0.06

5 Hydrodynamic Modeling for the 475 VTMAUV

Research and development on the 4.75 inch diameter Virginia Tech Miniature AUV (currently referred to as the 475) is currently underway. A USAERO model of the 475 can be seen in Figure 23. The grid pattern and panel distribution was developed in Surfgen, described in Section 3.3.1, in which the final representation was determined from a panel study.

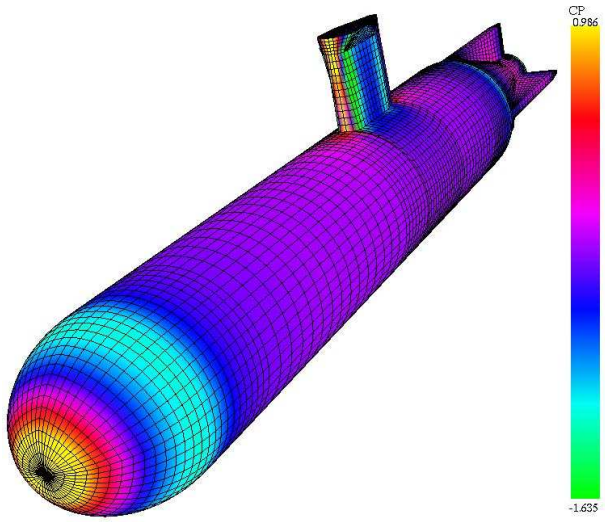

Figure 23: 475 Glider in USAERO/OMNI3D

One goal for the project is to understand the effects of adding circular cylinders (payloads) to the undercarriage of the model and determining the changes in added mass/inertia. There are to be several studies done with this model by adding several types of circular cylinders which vary in size, location, and diameter. For this thesis research contribution, only the added mass/inertia calculations are desired, as the viscous terms are to be determined by other researchers using a different CFD program.

There are three different configurations of the 475 that are being considered and analyzed in this research. The differences involve changing the location of the mast and the center of gravity on the vehicle. For naming purposes, one will be called the forward mast position, another the middle mast position, and the third the aft mast position.

The added mass/inertia matrices for the three configurations are given immediately, with the graphical solution following later. For the forward mast position the added mass/inertia matrix is represented in Equation (74) (Units are in English units). The middle mast position is represented in Equation (75). The aft mast position is represented in Equation (76).

$$\left[\begin{array}{c|c} \boldsymbol{M_f} & \boldsymbol{C_f}^T \\ \hline \boldsymbol{C_f} & \boldsymbol{I_f} \end{array}\right]_{\text{475ForwardMast}} = \begin{bmatrix} -0.032 & 0.000 & 0.000 & 0.000 & 0.000 & 0.000 \\ 0.000 & -0.639 & 0.000 & 0.0131 & 0.000 & 0.079 \\ 0.000 & 0.000 & -0.559 & 0.000 & -0.0618 & 0.000 \\ 0.000 & 0.0132 & 0.000 & -0.0035 & 0.000 & -0.0029 \\ 0.000 & 0.000 & -0.0619 & 0.000 & -0.280 & 0.000 \\ 0.000 & 0.0789 & 0.000 & -0.0029 & 0.000 & -0.285 \end{bmatrix} \tag{74}$$

$$\left[\begin{array}{c|c} \boldsymbol{M_f} & \boldsymbol{C_f}^T \\ \hline \boldsymbol{C_f} & \boldsymbol{I_f} \end{array}\right]_{\text{475MiddleMast}} = \begin{bmatrix} -0.032 & 0.000 & 0.000 & 0.000 & 0.000 & 0.000 \\ 0.000 & -0.649 & 0.000 & 0.013 & 0.000 & 0.088 \\ 0.000 & 0.000 & -0.559 & 0.000 & -0.059 & 0.000 \\ 0.000 & 0.0131 & 0.000 & -0.0035 & 0.000 & -0.005 \\ 0.000 & 0.000 & -0.059 & 0.000 & -0.279 & 0.000 \\ 0.000 & 0.090 & 0.000 & -0.0049 & 0.000 & -0.291 \end{bmatrix} \tag{75}$$

$$\left[\begin{array}{c|c} \boldsymbol{M_f} & \boldsymbol{C_f}^T \\ \hline \boldsymbol{C_f} & \boldsymbol{I_f} \end{array}\right]_{\text{475AftMast}} = \begin{bmatrix} -0.032 & 0.000 & 0.000 & 0.000 & 0.000 & 0.000 \\ 0.000 & -0.646 & 0.000 & 0.013 & 0.000 & 0.106 \\ 0.000 & 0.000 & -0.559 & 0.000 & -0.064 & 0.000 \\ 0.000 & 0.013 & 0.000 & -0.0035 & 0.000 & -0.0072 \\ 0.000 & 0.000 & -0.064 & 0.000 & -0.279 & 0.000 \\ 0.000 & 0.107 & 0.000 & -0.0071 & 0.000 & -0.302 \end{bmatrix} \tag{76}$$

The graphs below represent how the solution to the added mass/inertia and coupling matrices were obtained for each of the mast positions. The slopes of the lines in the graphs represent the terms of interest and are presented below.

Like *Slocum* and *XRay/Liberdade* gliders, we can compute the inertia matrix of the rigid body vehicle for each of these mast locations. These rigid body inertia matrices are calculated in Rhinoceros 3.0 as volume moment, and must be multiplied by density to get the proper units of slugs·ft^2. For the forward mast position the rigid body inertia is,

$$\boldsymbol{I}_{\mathbf{rb}} = \begin{bmatrix} 0.012 & 0 & 0 \\ 0 & 0.294 & 0 \\ 0 & 0 & 0.292 \end{bmatrix} \tag{77}$$

and for the middle mast position, it is

$$\boldsymbol{I}_{\mathbf{rb}} = \begin{bmatrix} 0.012 & 0 & 0 \\ 0 & 0.294 & 0 \\ 0 & 0 & 0.293 \end{bmatrix} \tag{78}$$

and for the aft mast position, it is

$$\boldsymbol{I}_{\mathbf{rb}} = \begin{bmatrix} 0.012 & 0 & 0 \\ 0 & 0.296 & 0 \\ 0 & 0 & 0.294 \end{bmatrix} \tag{79}$$

These values seem to remain almost constant in all three configurations because both the mast location and center of volume of the model are changing. As the mast location moves rearward, the center of volume also moves rearward. When the moments of inertia are recalculated for each case, they are all analyzed around different centers of volume. As the center of volume moves rearward when the mast moves rearward, more volume is accounted for in front of the center of mass, thus only slightly changing the net volume distribution

of the model. This explains why the values in the rigid body inertia matrices may not be drastically changing in relation to one another for each mast location study.

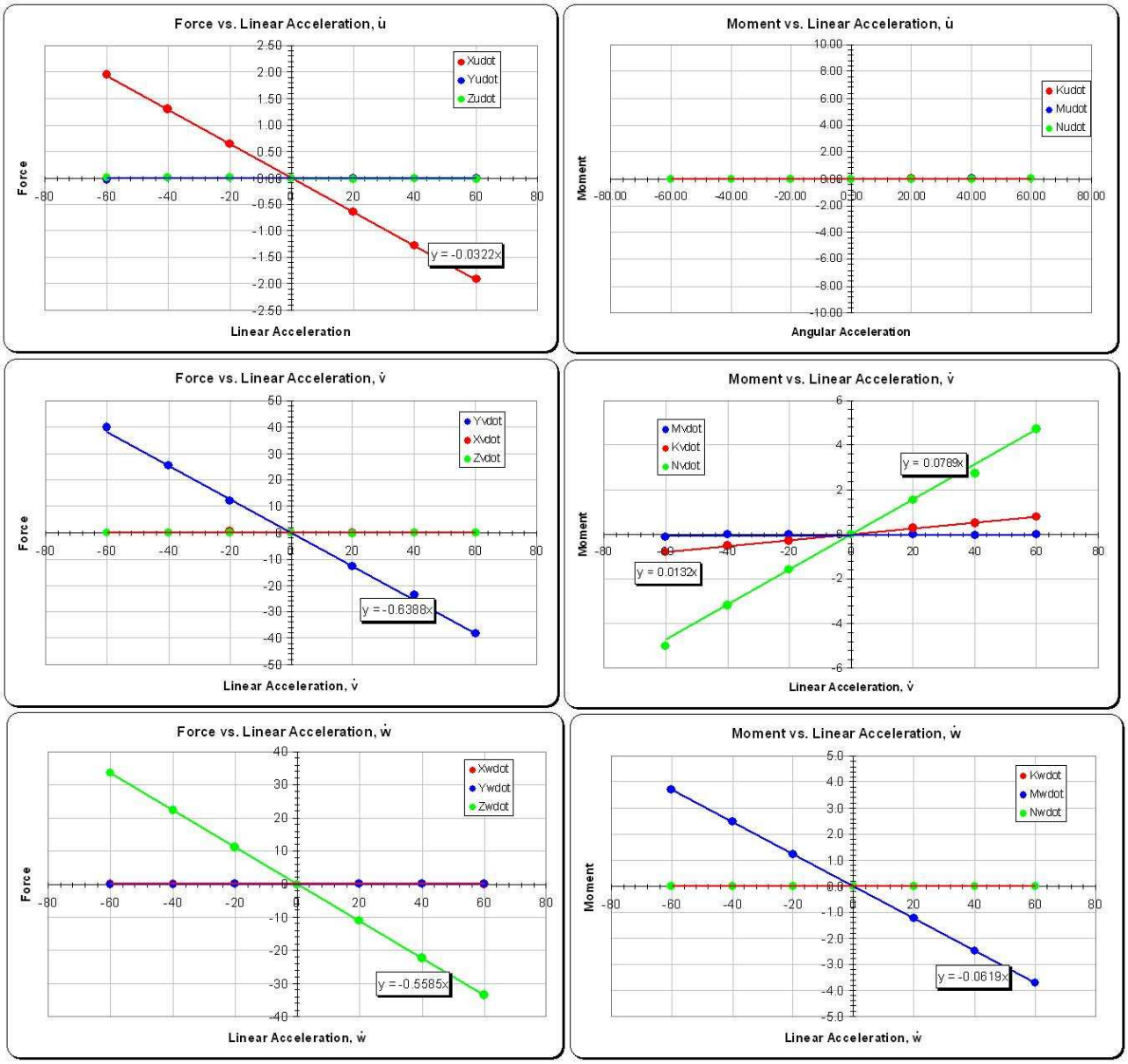

Figure 24: 475 Forward Mast Linear Acceleration Terms

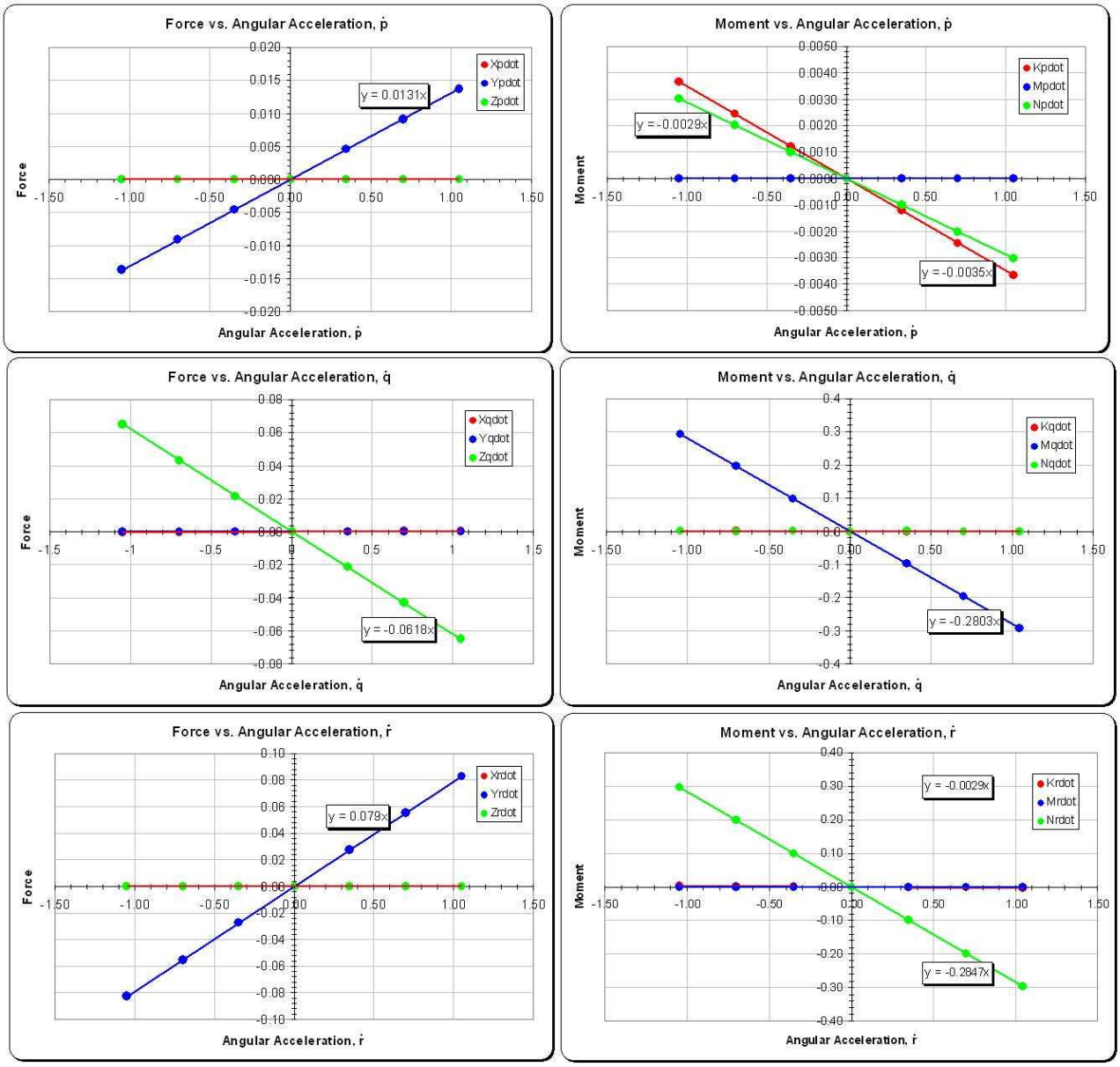

Figure 25: 475 Forward Mast Angular Acceleration Terms

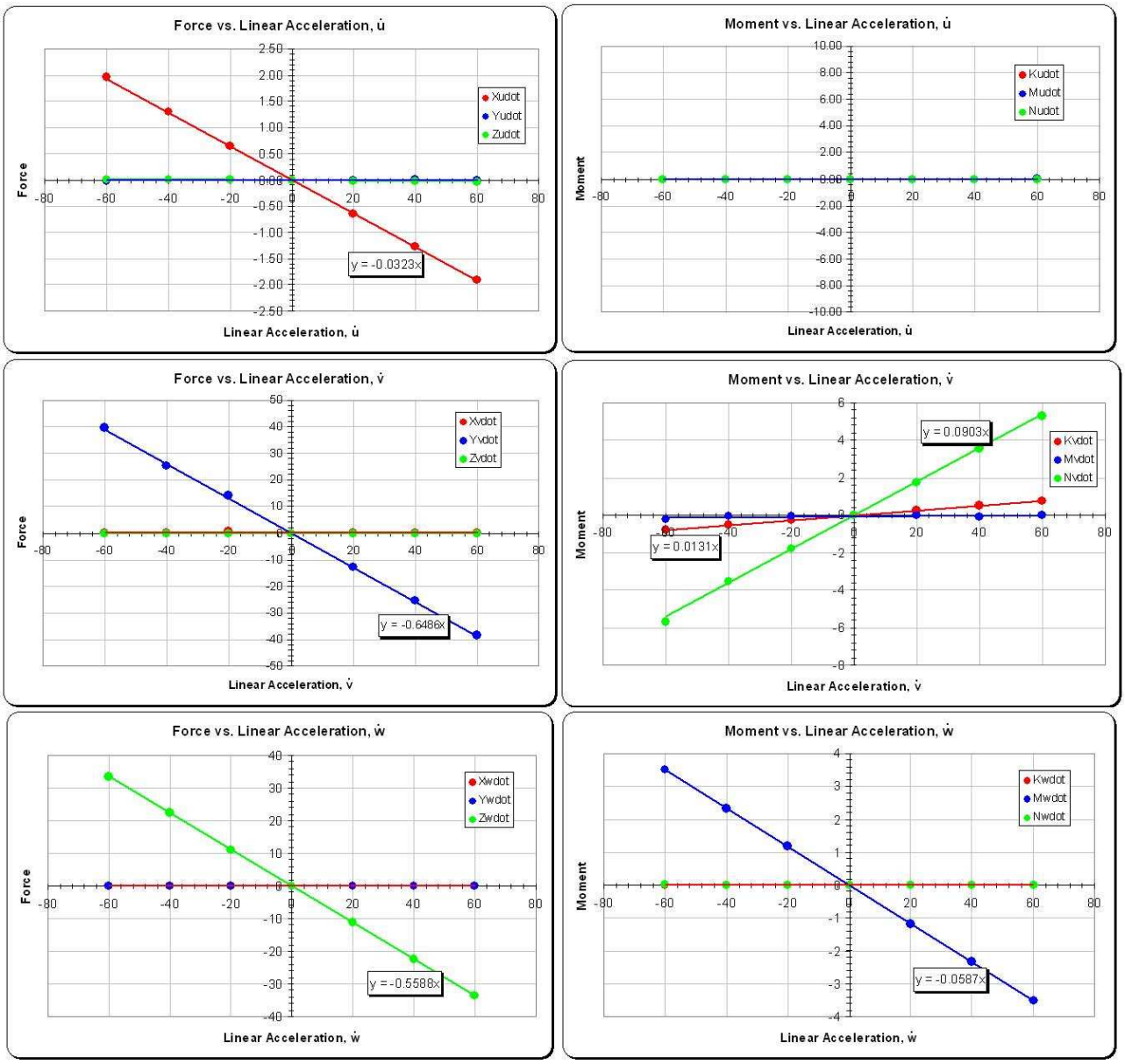

Figure 26: 475 Middle Mast Linear Acceleration Terms

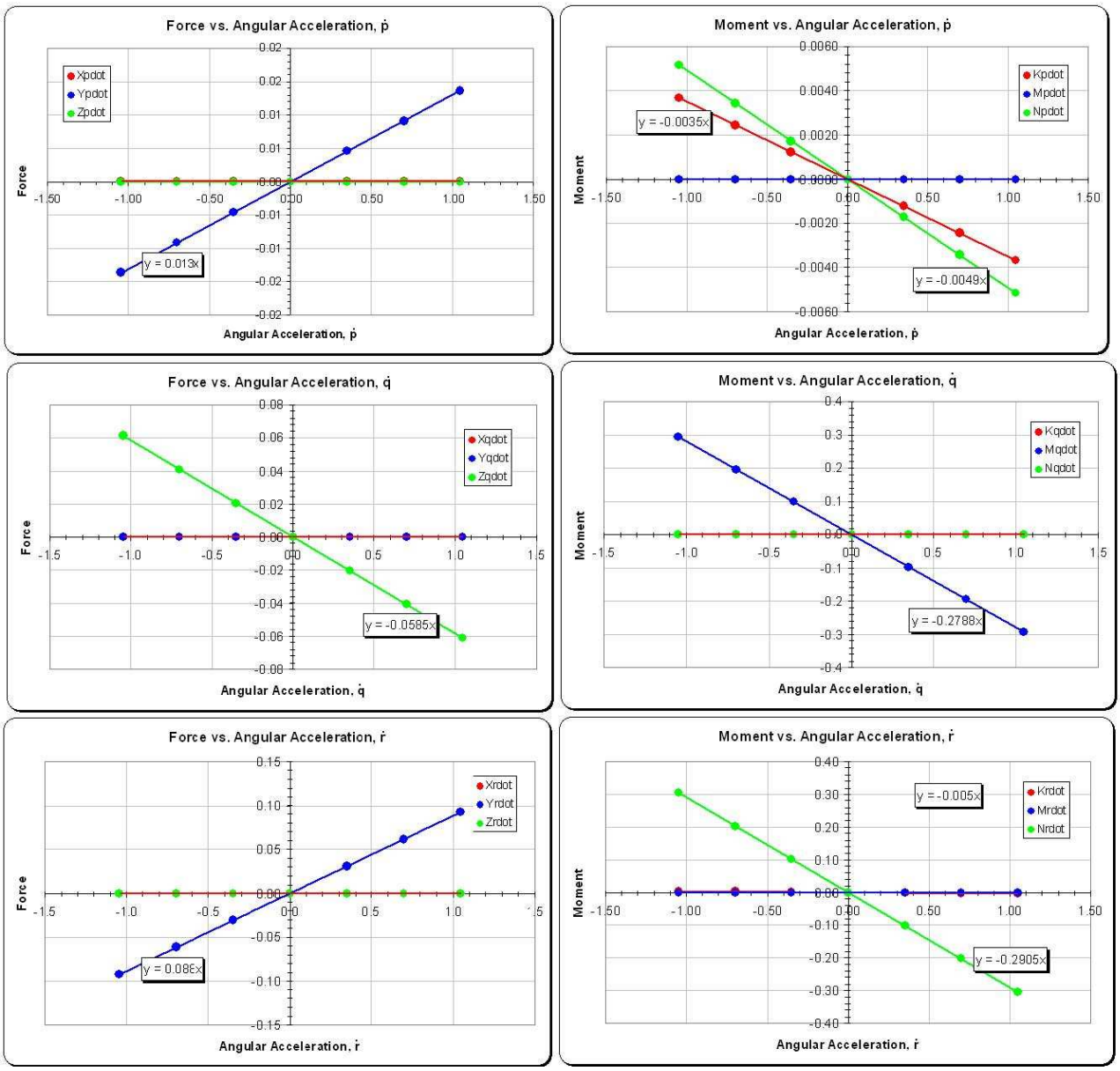

Figure 27: 475 Middle Mast Angular Acceleration Terms

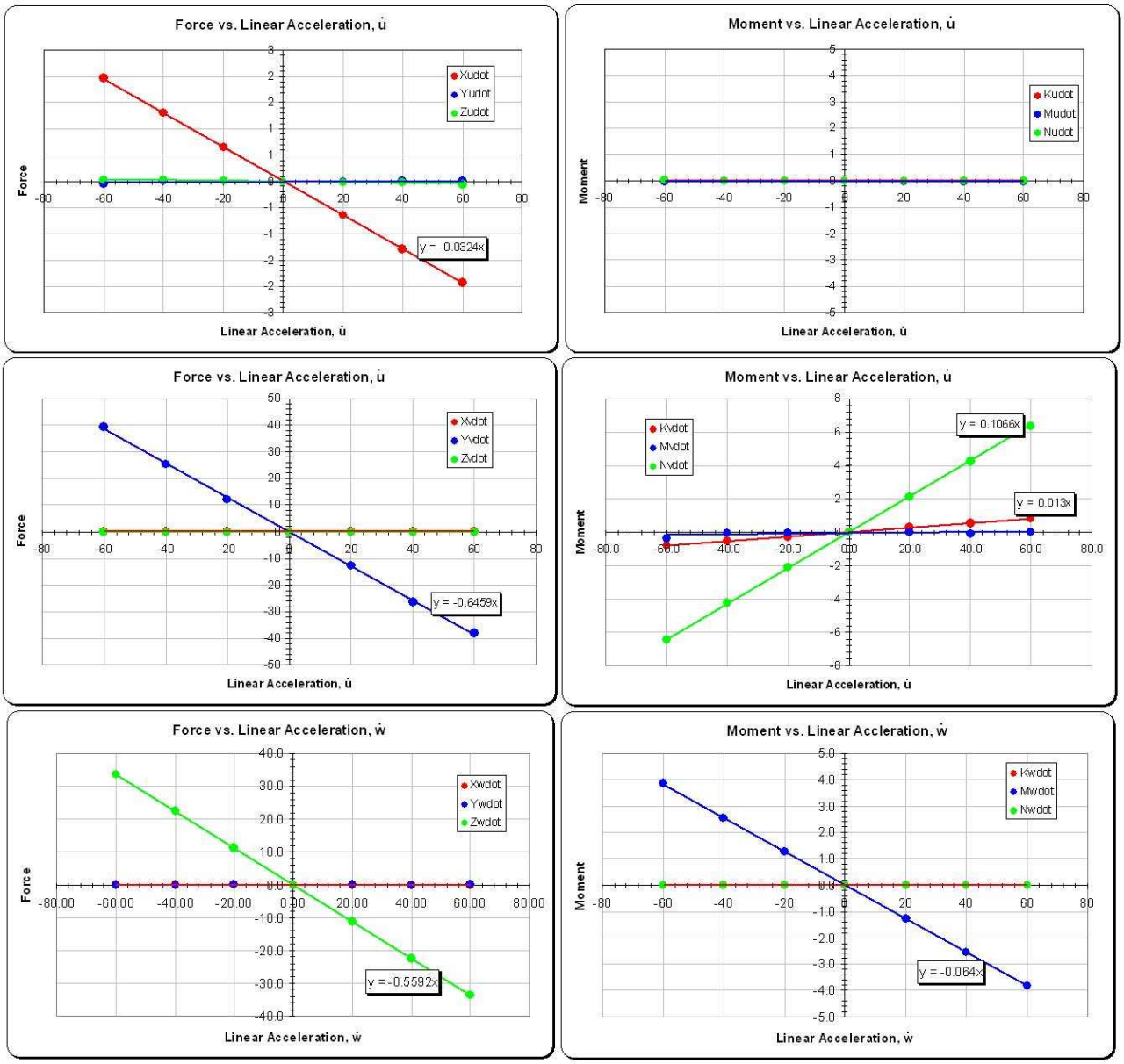

Figure 28: 475 Aft Mast Linear Acceleration Terms

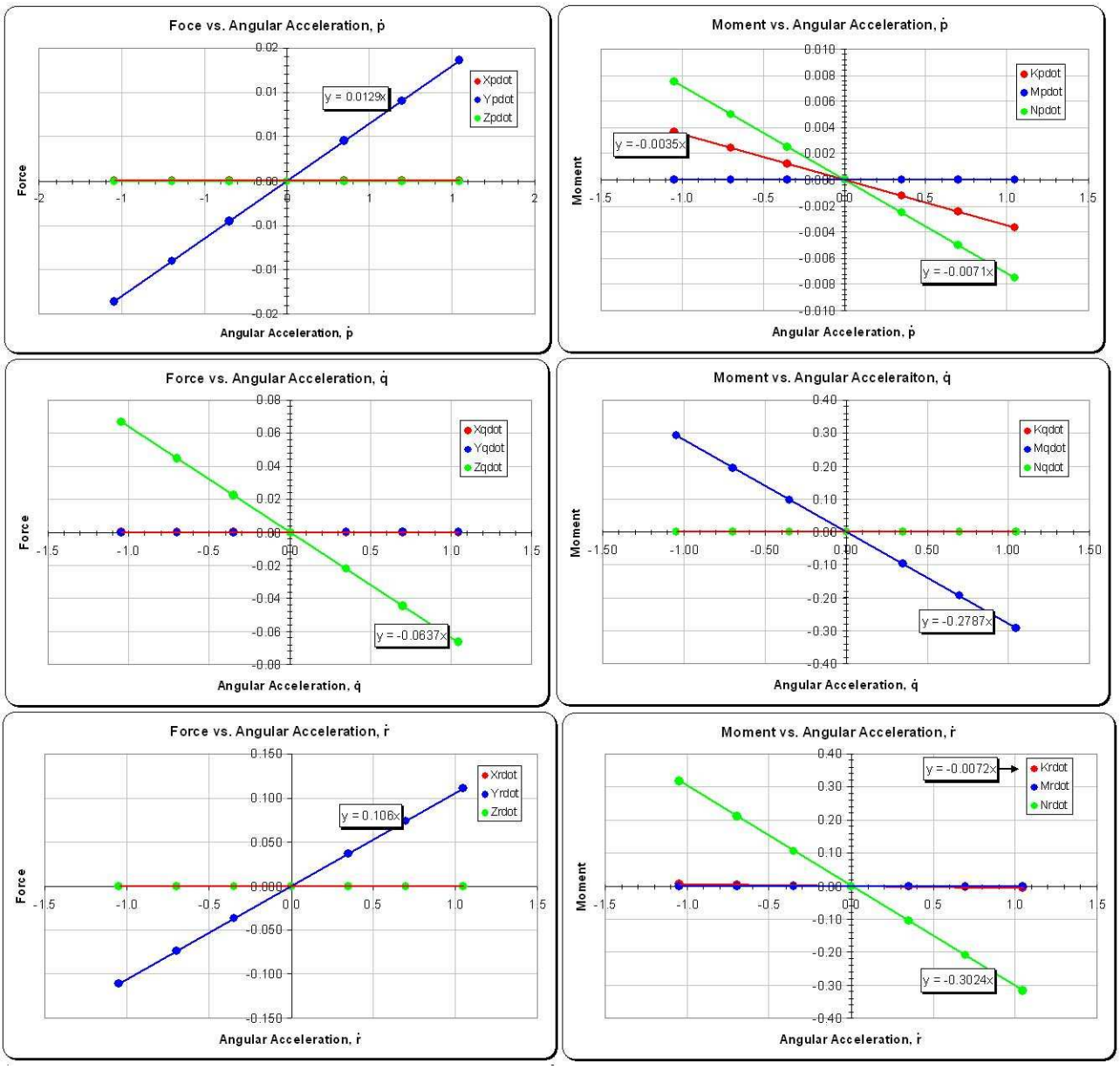

Figure 29: 475 Aft Mast Angular Acceleration Terms

6 Summary and Conclusions

Computational flight tests were performed on two buoyancy driven underwater gliders and one autonomous underwater vehicle. The study yielded the generalized inertia matrix for all three vehicles. The purpose of obtaining the generalized inertia matrix for the vehicles was to determine some of the hydrodynamic parameters which play a role in the governing equations of motion. For *Slocum*, the viscous parameters were also obtained. The hydrodynamic parameters for the *Slocum* glider have been completely determined.

Further, researchers at Virginia Tech are now equipped and capable of using, with confidence, the panelling program Surfgen, as well as the CFD program, USAERO. Future parameter studies can be performed for the models presented in this thesis, or new models. The same process of obtaining the hydrodynamic parameter solutions can be performed as outlined in this thesis.

6.1 Future Work and Recommendations

A goal for the 475 project is to determine the effects of adding different payloads of varying size, length, and location under the hull and determining the result in changing generalized inertia matrix of the system. This could provide a database of model parameter values for various sizes and locations of payloads.

Another area that this thesis did not handle was determining the viscous data for *XRay/Liberdade* and the 475. There is a current working project for the 475 to determine the viscous data using a separate CFD program, named Fluent. Viscous terms for the *XRay/Liberdade* glider have been computed using a CFD program by collaborators at SIO/MPL.

A Details of Semi-Empirical Calculations

The following information details how results obtained in Section 4 were achieved. The equations in this section are given in [13] and make use of the parameters listed in Table 7 in Section 4.

A.1 General Calculations

The following calculations are some basic calculations that will be called upon many times in process of obtaining the stability coefficients. Some of these values are for any type of motion and others are specific to a certain flight condition. For all calculations depending on either scenario, the parameters that can change due to flight conditions are all being set to the equilibrium parameter values determined from previous research on the *Slocum* glider [7].

Aspect ratio of the wing:

$$A = b^2/S = (3.21)^2/(1.43) = 7.21 \tag{80}$$

Aspect ratio of the tail:

$$A_{v_{eff}} = b_v^2/S_v = (0.52)^2/(0.32) = 0.87 \tag{81}$$

Taper ratio of the wing:

$$\lambda = c_t/c_r = (0.37)/(0.53) = 0.69 \tag{82}$$

Mach number of the vehicle:

$$M = V/a = (2.54/4921) = 0.0005 \tag{83}$$

Lift Coefficient:

$$C_L = \frac{W}{(1/2)\rho V^2 S} = \frac{110.2}{(1/2)(1.9905)(2.54)^2(1.43)} = 12.03 \tag{84}$$

Reynolds Number:

$$R = \frac{V \cdot l}{\nu} = \frac{(0.774)(5.898)}{1.924 \cdot 10^{-5}} \cong 237000 \tag{85}$$

A.2 Repeated Coefficients Calculations

Several of the calculations below make use of more complicated values or coefficients multiple times. Instead of repeating the calculation for each section, the calculation will be done once here to show where the values come from and then taken to the proper equation where it is called to solve for the more general coefficient.

$C_{L_{\alpha_w}}$. Several coefficients call upon the $C_{L_{\alpha_w}}$ coefficient, which is the wing lift curve slope. The process for obtaining this value starts in Chapter 8, Section 8.1.3.2, page 248 in Roskam [13]

$$C_{L_{\alpha_w}} = \frac{2\pi A}{\sqrt{2 + ((\frac{A^2\beta^2}{k^2})(1 + \frac{\tan^2 \Lambda_{c/4}}{\beta^2}) + 4)}} \tag{86}$$

where the aspect ratio, A is defined in Section A.1, and $\Lambda_{c/4}$ is the quarter-chord sweep angle of the wing. β and k are defined by the following:

$$\beta = (1 - M^2)^{(1/2)} \tag{87}$$

$$k = (C_{l_\alpha})_{atM}/2\pi \tag{88}$$

If it is assumed that the wing cross section on *Slocum* resembles the NACA 0009 airfoil, then from [13] $C_{l_\alpha} = 6.245$ [1/rad] and $k = 0.994$. Using the value for Mach number described in Section A.1, $\beta \approx 1$. Using these values for A, k, β, and $\Lambda_{c/2}$, the value for $C_{L_{\alpha_w}}$ to be used throughout the calculations comes to **3.73** [1/rad].

Another repeated calculation is the component of drag from the wing, which is determined from [12] using the following equation:

$$C_{D_{o_w}} = \frac{(C_{f_w})S_{wet_w}(FF_w)(Q_w)}{S} \tag{89}$$

where

$$C_{f_w} = \frac{1.328}{\sqrt{R_w}} = 0.01 \tag{90}$$

$$FF = [1 + \frac{0.6}{(x/c)_m}(\frac{t}{c}) + 100(\frac{t}{c})^4][1.34M^{0.18}(\cos\Lambda_m)^{0.28}] \tag{91}$$

Q can be assumed to be one. Plugging in the remaining surface and wetted surface area values, yields $C_{D_{0_w}}$ = **0.028**.

Another widely repeated calculation that is often used is the value for $C_{y_{\beta_v}}$, defined by the following equation:

$$C_{y_{\beta_v}} = -k_v(C_{L_{\alpha_v}})(1 + d\sigma/d\beta)\eta_v(S_v/S) \tag{92}$$

where k_v can be obtained from Figure 10.12 [13] as 1.0. $C_{L_{\alpha_v}}$ is obtained from 8.1.3.2 [13] in the same manner described for determining $C_{L_{\alpha_w}}$ except with substitution of $A_{v_{eff}}$ in place of A. Replacing A with $A_{v_{eff}}$ yields $C_{L\alpha_v}$ = 1.296 [1/rad]. Carrying out these calculations and plugging in the known parameters yields $C_{y_{\beta_v}}$ is equal to **-0.32**. A useful note to include is that for the *XRay/Liberdade* and *Slocum* gliders, $C_{y_{\beta_v}} \approx C_{y_\beta}$

Angle of attack is also called on in quite a few calculations. From Raymer, the angle of attack of choice would be the angle which provides the maximum lifting coefficient, or the highest lift to drag ratio.

$$C_{L_{max}} = 0.9 C_{l_{max}} \cos \Lambda_{c/4} \tag{93}$$

From Roskam, the value of $C_{l_{max}}$ is given as 1.32. Therefore, $C_{L_{max}} = 0.857$. Since C_{L_α} has already been calculated, α can be determined through the following:

$$C_{L_{max}} = C_{L_\alpha} \alpha \tag{94}$$

The maximum lift angle of attack is $\alpha = 13.2^o$

A.3 Viscous Coefficients Calculations

C_{L_α}: Lift-Due-To-Angle-of-Attack

This calculation starts in Chapter 8, Section 8.1.5.3, page 272 of Roskam [13].

$$C_{L_\alpha} = C_{L_{\alpha_{wf}}} + C_{L_{\alpha_h}} \eta_h (S_h/S)(1 - d\varepsilon/d\alpha) + C_{L_{\alpha_c}} \eta_c (S_c/S)(1 + d\varepsilon_c/d\alpha) \tag{95}$$

The equation above can be simplified since the *Slocum* has neither horizontal tail nor canard. This reduces the above equation to the following:

$$C_{L_\alpha} = C_{L_{\alpha_{wf}}} = K_{wf} C_{L_{\alpha_w}} \tag{96}$$

K_{wf} is the wing-fuselage interference factor determined from the following equation which calls upon parameters defined in Table 7:

$$K_{wf} = 1 + 0.025(d_f/b) - 0.25(d_f/b)^2 = 0.994 \tag{97}$$

With this value of K_{wf} and recalling the value for $C_{L_{\alpha_w}}$ from above, it can be shown that C_{L_α} is equal to **3.733**.

C_{m_α}: Pitching-Moment-Due-To-Angle-of-Attack

This equation starts in Chapter 8, Section 8.2.5.2, page 324 of Roskam [13]. The pitching moment due to angle of attack can be stated with the following equation:

$$C_{m_\alpha} = (\frac{dC_m}{dC_L})C_{L_\alpha} \tag{98}$$

To solve this, the airplane pitching moment variation with lift coefficient must be defined as the following:

$$dC_m/dC_L = \bar{x}_{ref} - \bar{x}_{ac_A} \tag{99}$$

$\bar{x}_{ref}$ can be determined from Figures 8.97b and 8.114 of [13], whose value can be determined exactly with Rhinoceros 3.0. The next step is obtaining the value of the location of the airplane aerodynamic center in fractions of the mean geometric center.

$$\bar{x}_{ac_A} = ((\bar{x}_{ac_{wf}})C_{L_{\alpha_{wf}}} + (\eta_h C_{L_{\alpha_h}}(1 - d\varepsilon/d\alpha)(S_h/s)\bar{x}_{ac_h} - \eta_c C_{L_{\alpha_c}}(1 + d\varepsilon_c/d\alpha)(S_c/S)\bar{x}_{ac_c}))/C_{L_\alpha} \tag{100}$$

Note again that the equation can be reduced since there is no horizontal tail nor canard present on the *Slocum*. Other useful equations are as follows:

$$\bar{x}_{ac_{wf}} = \bar{x}_{ac_w} + \Delta\bar{x}_{ac_f} \tag{101}$$

$$x_{ac_w} = n_{ac} - n_{mgc} = 0.11 \tag{102}$$

n_{ac} and n_{mgc} are defined in Figure 8.97a [13], which can again be determined from Rhinoceros 3.0. $C_{L_{\alpha_{wf}}}$ and C_{L_α} have both been defined above and can be replaced with their actual values here. Proceeding forward, the next useful equations are as follows:

$$\Delta x_{ac_f} = -(dM/d\alpha)/(\bar{q}S\bar{c}C_{L_{\alpha_w}}) \tag{103}$$

$$(dM/d\alpha) = (\bar{q}/36.5)(C_{L_{\alpha_w}}/0.08)_{i=1}^{i=13}[\sum((w_{f_i})^2(d\bar{\varepsilon}/d\alpha)_i\Delta x_i)] \tag{104}$$

Note, w_{f_i} and Δx_i are defined as average width and spacing at each cross-section of interest, respectively. $C_{L_{\alpha_w}}$ has been calculated previously. $(d\bar{\varepsilon}/d\alpha)_i$ can be interpreted from Figure 8.115 and 8.116 [13]. Note, for *Slocum*, only the sections in front of wing are relevant since there is no horizontal tail. After taking out the necessary calculations for *Slocum*, $(dM/d\alpha) = 0.059\bar{q}$. Plugging this value into the Δx_{ac_f} equation above, cancelling the $\bar{q}$ values, and plugging in the value for $C_{L_{\alpha_w}}$ described earlier yields $\Delta\bar{x}_{ac_f} = -0.66$. This leads to $\bar{x}_{ac_{wf}} = \bar{x}_{AC_A} = -0.407$. This then yields $(dC_m/dC_L) = -0.54$ which can finally be submitted into the starting equation and after proper scaling gives the final result as C_{m_α} equal to **-0.1459**.

C_{l_β}: Rolling-Moment-Due-To-Sideslip

This calculation starts in Chapter 10, in section 10.2.4, on page 389 of [13].

$$C_{l_\beta} = C_{l_{\beta_{wf}}} + C_{l_{\beta_h}} + C_{l_{\beta_v}} \tag{105}$$

The above equation can be slightly modified since there is no horizontal tail on the *Slocum* model. Analyzing the first term of the above equation can be done with the following equation:

$$C_{l_{\beta_{wf}}} = 57.3(C_{L_{wf}}((C_{l_\beta}/C_L)_{\Lambda_{c/2}}(K_{M_\Lambda})(K_f) + (C_{l_\beta}/C_L)_A) + \Gamma((C_{l_\beta}/\Gamma)K_{M_\Gamma} + (\Delta C_{l_\beta}/\Gamma)) + (\Delta C_{l_\beta})_{z_w} + (\varepsilon_t \tan\Lambda_{c/4})((\Delta C_{l_\beta})/\varepsilon_t \tan\Lambda_{c/4})) \tag{106}$$

For preliminary design purposes, $C_{L_{wf}} = C_L$. Next, $(C_{l_\beta}/C_L)_{\Lambda_{c/2}}$ can be obtained from Figure 10.20 of [13], and is -0.0045 [1/deg]. K_{M_Λ} can be obtained from Figure 10.21 of [13], and is 1. K_f is obtained from Figure 10.22 of [13], and is 0.5. $(C_{l_\beta}/C_L)_A$ is obtained from Figure 10.23 of [13], and is -0.001 [1/deg]. And finally, Γ can be obtained from Figure 10.7 of [13]. Note, for *Slocum*, $\Gamma = \varepsilon_t = 0$. Another component in the above equation can be defined with the following equation:

$$(\Delta C_{l_\beta})_{z_w} = 0.042(A)^{(1/2)}(z_w/b)(d_{f_{ave}}/b) \tag{107}$$

Using z_w as defined in Figure 10.9 of [13], the equation above goes to zero and the equation for $C_{l_{\beta_{wf}}}$ is dramatically simplified. Using the values obtained from the figures for the components of the equation, $C_{l_{\beta_{wf}}} = -2.29$. The contribution from the vertical tail can be determined from the following equation:

$$C_{l_{\beta_v}} = (C_{y_{\beta_v}})(z_v \cos\alpha - l_v \sin\alpha)/b \tag{108}$$

Here, $C_{y_{\beta_v}}$ is from Equation 10.28 of [13], and has been solved above. z_v and l_v are both determined from Figure 10.27 of [13], and are listed in Table 7. Plugging in these values yields $C_{l_{\beta_v}} = -0.034$. Combining the wing-fuselage interaction and vertical tail terms from the starting equation and properly scaling gives a final value for C_{l_β} equal to **-1.427**.

C_{n_β} Yawing-Moment-Due-To-Sideslip

This calculation starts in Chapter 10, Section 10.2.4, on page 397 of [13]. This value is comprised of the following components:

$$C_{n_\beta} = C_{n_{\beta_w}} + C_{n_{\beta_f}} + C_{n_{\beta_v}} \tag{109}$$

$C_{n_{\beta_w}}$ is defined from DatCom [4] through:

$$C_{n_{\beta_w}} = C_L^2[\frac{1}{4\pi A} - \frac{\tan\Lambda_{c/4}}{\pi A(A + 4\cos\Lambda_{c/4})}[\cos\Lambda_{c/4} - \frac{A}{2} - \frac{A^2}{8\cos\Lambda_{c/4}} + \frac{6\bar{x}\sin\Lambda_{c/4}}{A\bar{c}}]] = 8.908 \tag{110}$$

$$C_{n_{\beta_f}} = -57.3K_N K_{R_1}(S_{f_s} l_f / Sb) \tag{111}$$

K_N can be determined from Figure 10.28 of [13], and is 0.0015. K_{R_1} can be determined from Figure 10.29 of [13], and is 1. S_{f_s} and l_f are defined from Figure 10.28 of [13], and can be calculated exactly with Rhinoceros 3.0. The vertical tail contribution is given by the following:

$$C_{n_{\beta_v}} = -(C_{y_{\beta_v}})(l_v \cos\alpha + z_v \sin\alpha)/b \tag{112}$$

where $C_{y_{\beta_v}}$ is determined from Equation 10.28 of [13], calculated above. l_v and z_v are again from Figure 10.27 of [13]. Plugging in the necessary components to the parameters and coefficients described here and properly scaling yields C_{n_β} is equal to **4.845**.

C_{y_p} Side-Force-Due-To-Roll-Rate

This equation starts in Chapter 10, Section 10.2.6, on page 417 of [13]. It is defined by the following equation:

$$C_{y_p} = 2(C_{y_{\beta_v}})(z_v \cos\alpha - l_v \sin\alpha)/b \tag{113}$$

where $C_{y_{\beta_v}}$ can be determined from Equation 10.28 of [13], described above. z_v and l_v are determined from Figure 10.27 of [13], which can be computed exactly in Rhinoceros 3.0. Plugging in these values and multiplying by the nondimensionaled correction factor yields C_{y_p} is equal to **0.103**.

C_{l_p} Rolling-Moment-Due-To-Roll-Rate

This equation starts in Chapter 10, Section 10.2.6, on page 417 of [13]. It is defined by the following equation:

$$C_{l_p} = C_{l_{p_w}} + C_{l_{p_h}} + C_{l_{p_v}} \tag{114}$$

Since there is no horizontal tail component on *Slocum*, this equation can simplify slightly. Analyzing the remaining first component can be done with the following equation:

$$C_{l_{p_w}} = (\beta C_{l_p}/k)_{C_L=0}(k/\beta)((C_{l_{\alpha_w}})_{C_L}/(C_{L_{\alpha_w}})_{C_L=0})((C_{l_p})_\Gamma/(C_{l_p})_{\Gamma=0}) + (\Delta C_{l_p})_{drag} \tag{115}$$

where $(\beta C_{l_p}/k)_{C_L=0}$ can be obtained from Figure 10.35 of [13], and is -0.4. Note, in this equation the following parameters need to be redefined:

$$\beta = (1 - M^2)^{(1/2)} \tag{116}$$

$$k = (C_{l_\alpha})_M \beta/2\pi \tag{117}$$

Here, $(C_{L_{\alpha_w}})_{C_L=0}$ can be obtained from Equation 8.22 of [13] and is worked out in an earlier section. $(C_{l_{\alpha_w}})_{C_L}$ can be calculated from Section 8.1.3.5 of [13] and has been previously defined. z_w can be obtained from Figure 10.9 of [13] and Γ from Figure 10.7 of [13]; both

which show their respective values to equal zero. The wing drag contribution to roll damping is given by:

$$(\Delta C_{l_p})_{drag} = ((C_{l_p})_{C_{D_L}}/(C_{L_w})^2)(C_{L_w})^2 - 0.125C_{D_{o_w}} \tag{118}$$

where $(C_{l_{\alpha_w}})_{C_L}$ can be obtained from Figure 10.36 of [13], and is 1. Again, it is appropriate to set $C_{L_w} = C_L$. The remaining component, $C_{D_{o_w}}$, is obtained from Raymer [12] and is determined previously. The remaining component is the vertical tail contribution, determined from the following:

$$C_{l_{p_v}} = 2(z_v/b)^2 C_{y_{\beta_v}} \tag{119}$$

where z_v is obtained from Figure 10.27 of [13] and $C_{y_{\beta_v}}$ is determined from Equation 10.28 of [13], described earlier. Combining the vertical tail and wing sections and properly scaling yields C_{l_p} is equal to **-0.778**.

C_{n_p} Yawing-Moment-Due-To-Roll-Rate

This calculation starts in Chapter 10, Section 10.2.6, on page 421 of [13]. It is defined by the following equation:

$$C_{n_p} = C_{n_{p_w}} + C_{n_{p_v}} \tag{120}$$

The wing contribution is given by:

$$C_{n_{p_w}} = -((C_{n_p}/C_L)_{C_L=0,M})C_L + (C_{n_p}/\varepsilon_t)\varepsilon_t + ((\Delta C_{n_p}/\alpha_{\delta_f})(\delta_f))(\alpha_{\delta_f})\delta_f \tag{121}$$

where:

$$(C_{n_p}/C_L)_{C_L=0,M} = (\frac{A+4\cos\Lambda_{c/4}}{AB+4\cos\Lambda_{c/4}})(\frac{AB+(1/2)(AB+\cos\Lambda_{c/4})\tan^2\Lambda_{c/4}}{A+(1/2)(A+\cos\Lambda_{c/4})\tan^2\Lambda_{c/4}})(C_{n_p}/C_L)_{C_L=M=0} \tag{122}$$

where:

$$B = (1-M^2(\cos\Lambda_{c/4})^2)^{1/2} \tag{123}$$

and:

$$(C_{n_p}/C_L)_{C_L=M=0} = -\frac{1}{6}\frac{A+6(A+\cos\Lambda_{c/4})((\bar{x}/\bar{c})(\tan\Lambda_{c/4}/A)+(\tan^2\Lambda_{c/4}/12))}{A+4\cos\Lambda_{c/4}} \tag{124}$$

For the *Slocum* glider there is no wing twist contribution, ε_t, or flap deflection, δ_f, due to the construction design. Thus, the equation for the wing contribution term simplifies, and after plugging in the known parameters yields a value of -3.752. The vertical tail contribution is given by the following equation:

$$C_{n_{p_v}} = -(2/b^2)(l_v\cos\alpha + z_v\sin\alpha)(z_v\cos\alpha - l_v\sin\alpha - z_v)C_{y_{\beta_v}} \tag{125}$$

where z_v and l_v are obtained from Figure 10.27 of [13] and $C_{y_{\beta_v}}$ is determined from Equation 10.28 of [13], described above. Plugging in the necessary values yields $C_{n_{p_v}} = -0.242$. Combining the wing and tail contributions and properly scaling yields C_{n_p} =**-1.186**.

C_{m_q} Pitching-Moment-Due-To-Pitch-Rate

This calculation comes from the DatCom [4] reference CD which can be found in part 2 on page 193. It is defined by the following equation:

$$C_{m_q} = C_{m_{q_w}} + C_{m_{q_h}} + C_{m_{q_c}} \tag{126}$$

Since there is no horizontal tail or canard, the terms simplifies down to be equal to the wing contribution component, which is determined from the following equation:

$$C_{m_{q_w}} = -k_w C_{l_{\alpha_w}} \cos\Lambda_{c/4}(\frac{A(0.5(\bar{x}/\bar{c}) + 2(\bar{x}/\bar{c})^2)}{A + 2\cos\Lambda_{c/4}} + (1/24)\frac{A^3\tan^2\Lambda_{c/4}}{A + 6\cos\Lambda_{c/4}} + (1/8)) \quad (127)$$

Where k_w is determined from Figure 10.40 of [13], and is 0.71. In this equation, $\bar{x}$ is redefined through Figure 10.39 of [13], and is 0.512 ft. Plugging in the known parameters listed in the beginning table and properly scaling yields C_{m_q} =**-0.044**.

C_{y_r} Side-Force-Due-To-Yaw-Rate

This calculation starts in Chapter 10, Section 10.2.8, on page 428 of [13]. It is defined with the following equation:

$$C_{y_r} = -2(C_{y_{\beta_v}})(l_v cos\alpha + z_v sin\alpha)/b \quad (128)$$

where l_v and z_v is obtained from Figure 10.27 of [13] and $C_{y_{\beta_v}}$ from Equation 10.28 of [13], determined earlier. Plugging in these known values and properly scaling yields C_{y_r} is equal to **0.447**.

C_{l_r} Rolling-Moment-Due-To-Yaw-Rate

This calculation starts in Chapter 10, Section 10.2.8, on page 428 of [13]. It is defined with the following equation:

$$C_{l_r} = C_{l_{r_w}} + C_{l_{r_v}} \quad (129)$$

The wing contribution term can be determined from the following equation:

$$C_{L_{r_w}} = (C_{L_w})(C_{l_r}/C_L)_{C_L=0,M} + (\Delta C_{l_r}/\Gamma)\Gamma + (\Delta C_{l_r}/\varepsilon_t)\varepsilon_t + (\Delta C_{l_r}/\alpha_{\delta_f})(\alpha_{\delta_f})\delta_f \tag{130}$$

As stated earlier, there is no dihedral, Γ, wing twist, ε_t, or flap deflection, δ_f. Thus the equation is dramatically reduced. The slope of the rolling moment due to roll rate at zero lift is determined by the following equation:

$$(C_{l_r}/C_L)_{C_L=0,M} = \frac{1 + \frac{A(1-B^2)}{2B(AB+2\cos\Lambda_{c/4})} + \frac{AB+2\cos\Lambda_{c/4}}{AB+4\cos\Lambda_{c/4}}\frac{\tan^2\Lambda_{c/4}}{8}}{1 + \frac{AB+2\cos\Lambda_{c/4}}{AB+4\cos\Lambda_{c/4}}\frac{\tan^2\Lambda_{c/4}}{8}}(C_{l_r}/C_L)_{C_L=M=0} \tag{131}$$

where:

$$B = (1 - M^2(\cos\Lambda_{c/4})^2)^{(1/2)} \tag{132}$$

$(C_{l_r}/C_L)_{C_L=M=0}$ is determined from Figure 10.41 of [13], which is 0.45, and C_{L_w} from Equation 10.57 of [13], which has been previously determined. The wing contribution is determined as 5.533. The vertical tail contribution is determined from the following equation:

$$C_{l_{r_v}} = -(2/b^2)(l_v\cos\alpha + z_v\sin\alpha)(z_v\cos\alpha - l_v\sin\alpha)C_{y_{\beta_v}} \tag{133}$$

where z_v and l_v are obtained from Figure 10.27 of [13] and $C_{y_{\beta_v}}$ from Equation 10.28 of [13], which has been determined previously. Plugging in these known values and solving for the two components and properly scaling yields C_{l_r} is equal to **1.62**.

C_{n_r} Yawing-Moment-Due-To-Yaw-Rate

This equation starts in Chapter 10, Section 10.2.8, on page 432 of [13]. It is defined with the following equation:

$$C_{n_r} = C_{n_{r_w}} + C_{n_{r_v}} \tag{134}$$

The wing contribution term can be obtained with the following equation:

$$C_{n_{r_w}} = (C_{n_r}/C_L^2)(C_{L_w})^2 + (C_{n_r}/C_{D_o})C_{D_{o_w}} \tag{135}$$

where (C_{n_r}/C_L^2) is obtained from Figure 10.44 of [13], and is 0, and (C_{n_r}/C_{D_o}) from Figure 10.45 of [13], which is -0.5. C_{L_w} is determined from Equation 10.57 of [13], described earlier. $C_{D_{o_w}}$ is obtained from equations in from [12], also described earlier. Plugging the necessary values in shows that the wing contribution term is equal to -0.0014. The next component is the vertical tail contribution, given by the following equation:

$$C_{n_{r_v}} = (2/b^2)(l_v \cos\alpha + z_v \sin\alpha)^2 C_{y_{\beta_v}} \tag{136}$$

where z_v and l_v are obtained from Figure 10.27 of [13] and $C_{y_{\beta_v}}$ from Equation 10.28 of [13], which has been determined previously. Plugging in these known values and solving for the two components yields C_{n_r} is equal to **-0.062**.

B *Slocum* Study Results

B.1 *Slocum* Panel Study

The *Slocum* glider panel study was similar to the VTMAUV panel study in the sense that there were several places under review to determine the change in pressure coefficient due to change in panel density. For the *Slocum* glider, there were seven places under review: the nose, nose/body interaction, pre-wing body, location on front of wing, aft wing/end section interaction, location close to the end, and a location near the front of the tail section. Like the other glider panel studies, there were certain cases where not only the longitudinal panels needed to be increased, but also the panels defined in the y-z plane to avoid some panels becoming too high in aspect ratio. For this case, this did not affect the data drastically.

Table 9: Panel Distribution Over *Slocum* Body

Case	Nose	Nose/Body	MB	WB	WLE	Aft/Tail	MA	Boom/Tail	TLE
1	8	3	9	5	12	4	8	6	7
2	10	4	11	7	14	5	10	7	8
3	12	5	13	9	16	6	12	8	9
*4	14	6	15	11	18	7	14	9	10
5	16	7	17	13	20	8	15	10	11
*6	18	8	19	15	22	9	16	11	12
7	20	9	21	17	24	10	17	12	13

Here, "MB" refers to a mid-body location, "WLE" refers to the wing leading edge location, "MA" refers to the mid-aft location, and "TLE" refers to the tail leading edge location. The cases in Table 9 which have a * by the number indicate the studies that had an increase in panels in the y-z plane to reduce panels from becoming too large in aspect ratio. After each of these seven cases were built in Surfgen, they were ran in the CFD program USAERO and the following pressure coefficients were obtained at the various locations.

Table 10: Panel Distribution Over *Slocum* Body

Case	Nose Tip	Nose/Body	MB	FW	Aft/Tail	AEB	Frontal Tail
1	0.7206	-0.1737	-0.02477	-0.04189	-0.14248	0.65376	-0.17027
2	0.83603	-0.19248	-0.02504	-0.0486	-0.12334	0.71353	-0.21029
3	0.83579	-0.19773	-0.02841	-0.05594	-0.12097	0.76432	-0.23429
4	0.84373	-0.20409	-0.02824	-0.06247	-0.10938	0.94903	-0.27108
5	0.83953	-0.20683	-0.02811	-0.06934	-0.09341	0.93377	-0.29386
6	0.83784	-0.21392	-0.02855	-0.07139	-0.0777	0.9251	-0.3019
7	0.83847	-0.21463	-0.02846	-0.07086	-0.07389	0.94191	-0.30505

Here, "MB" refers to a mid-body location, "FW" refers to a frontal wing location, and "AEB" refers to an aft-end body location. The data in Table 10 can be represented graphically to better indicate how many panels should be defined over the vehicle. This can be seen in Figure 30.

After looking at several of the cases presented in Figure 30, the following conclusions can be drawn about the number of panels to define in each section to ensure proper panel distribution to capture the effects in the flow.

Nose	Nose/Body	MB	WB	WLE	Aft/Tail	AE	Boom/Tail	TLE
16	9	15	13	24	9	14	12	13

Table 11: Final Panel Distribution for *Slocum*

Here, "MB" refers to a mid-body location, "WB" refers to a wing body location, "WLE" refers to the wing leading edge location, "AE" refers to an aft-edge location, and "TLE" refers to a tail-leading edge location.

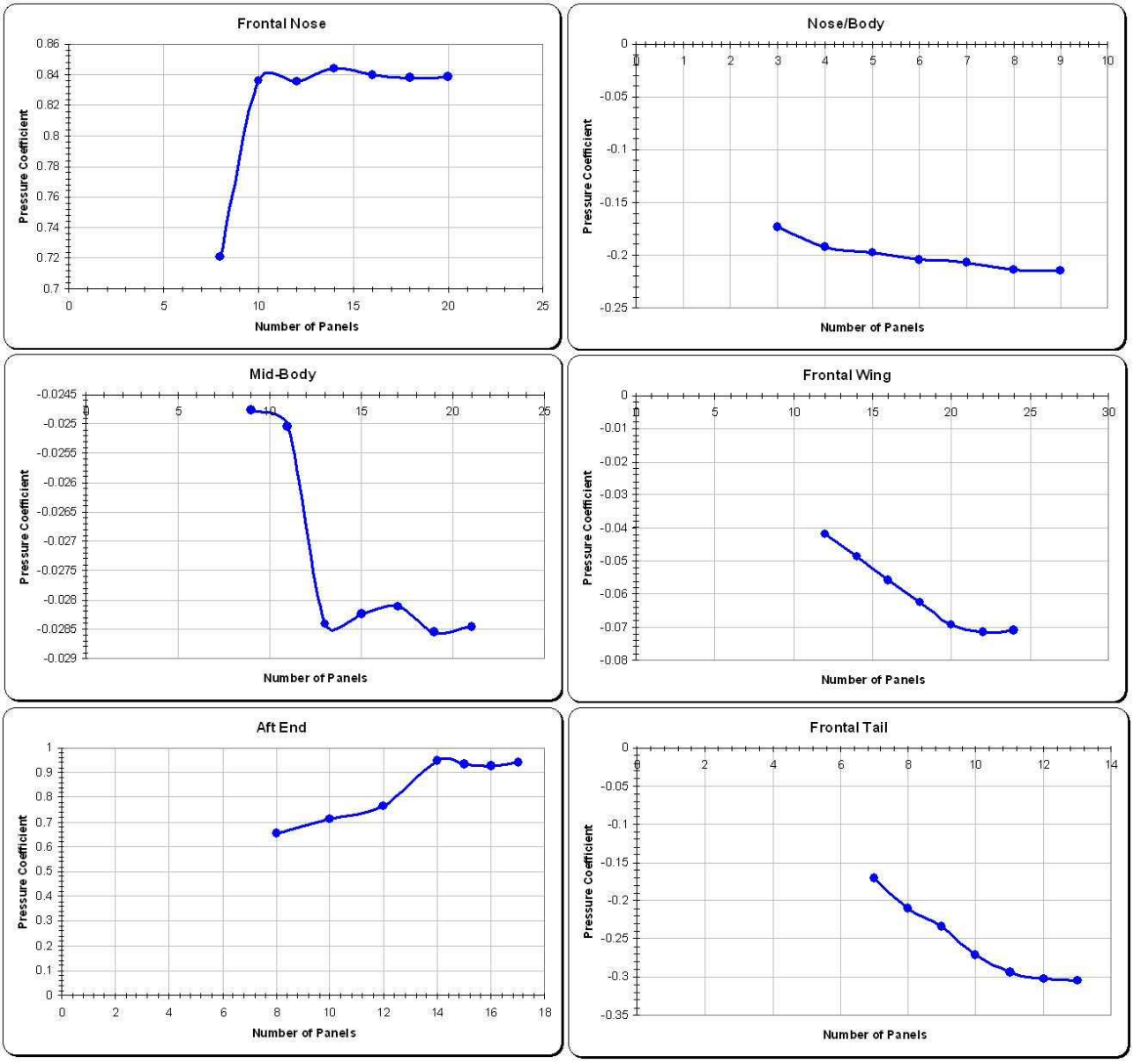

Figure 30: *Slocum* Panel Study

C *XRay/Liberdade* Study Results

C.1 *XRay/Liberdade* Panel Study

The *XRay/Liberdade* panel study was more difficult to perform than the *Slocum* and VT-MAUV panel studies due the geometry configuration. Defining more panels on the body automatically placed more panels on the end tails, and thus there was a run-time limit on the necessary number of panels to define on the the body. The panel study shows six cases that were ran in order to determine the changing pressure coefficients. The six locations under review were: nose tip, frontal body location (i.e. location close to the leading edge of the body), rear body location (i.e. location close to the trailing edge), central center tail location, side fin top frontal location, and side fin bottom frontal location.

Table 12: Panel Distribution Over *XRay/Liberdade* Body

Case	Nose	Mid Tail Fin	BCL	TST	BST	Body Frontal Location
1	4 and 3	5 and 4	9 and 13	6	3	20
2	6 and 4	7 and 5	12 and 17	8	4	30
3	10 and 4	9 and 5	15 and 20	11	5	40
4	13 and 5	12 and 6	18 and 24	13	6	50
5	16 and 5	15 and 6	21 and 27	16	8	60

Here, "BCL" refers to the body centerline location, "TST" refers to a top side tail location, and "BST" refers to a bottom side tail location. In Table 12, some locations have two panel numbers because they needed to be defined in the longitudinal and horizontal direction in order to maintain panel aspect ratios close to a value of one. Further, on the body centerline, (CL), two panel numbers are defined for the top and bottom body connectors on the centerline which control the number of panels. These are asymmetric due to the presence of the centerline tail. The pressure coefficient results of the panel study are shown below

Here, "FB" refers to the frontal body location. "RB" refers to the rear body location. "FCT"

Table 13: Pressure Distribution Over *XRay/Liberdade* Body per Study

Case	Nose	FB	RB	FCT	Frontal Top Tail	Frontal Bottom Tail
1	0.90899	0.60364	0.32025	-0.02157	0.60347	-0.15831
2	0.91398	0.66089	0.37567	0.04238	0.6298	-0.01141
3	0.91586	0.68063	0.42855	0.04512	0.66022	0.02966
4	0.91639	0.68405	0.43675	0.04813	0.66898	0.03356
5	0.91676	0.6873	0.43985	0.05217	0.67659	0.04551

refers to the frontal centerline tail location. The data in Table 13 can be represented in graphical form (Figure 31) to show the results used to determine the final panel distribution for the *XRay/Liberdade*.

Based on the graphs in Figure 31, the final panel distribution was determined and the solution is represented in Table 14.

Nose	Mid Tail Fin	Frontal Body	Body CL	Top Side Tail	Bottom Side Tail
13 and 5	10 and 5	40	16 and 21	15	5

Table 14: Final Panel Distribution on the *XRay/Liberdade* Body

Vita

Jesse Geisbert was born on July 30th, 1983 in Alexandria, Minnesota. He attended La Plata High School in Southern Maryland before attending Virginia Tech. He earned two undergraduate degrees in Aerospace and Ocean Engineering at Virginia Tech before starting his master's degree in the fall of 2005.

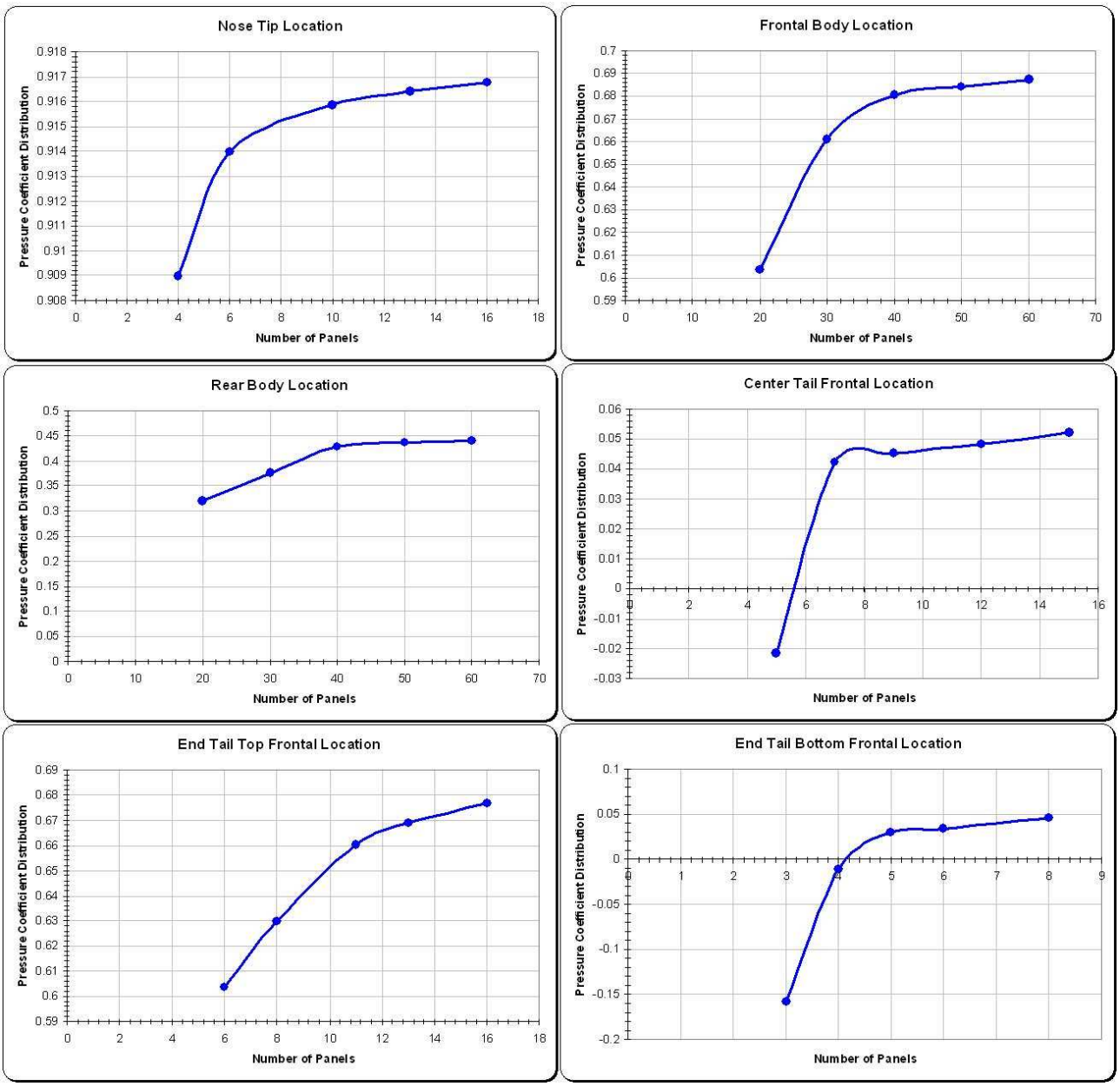

Figure 31: *XRay/Liberdade* Panel Study

References

[1] Analytical Methods, Inc., Redmond, Washington 98052. *USAERO. A Time-Stepping Analysis Method for the Flow About Multiple Bodies in General Motion*, version 4.2 edition, 2002.

[2] P. Bhatta. *Nonlinear Stability and Control of Gliding Vehicles.* PhD thesis, Princeton University, September 2006.

[3] Science Daily. Underwater glider makes history crossing gulf stream. (`http://www.sciencedaily.com/releases/2004/11/041108012708.htm`), November 2004.

[4] D. E. Ellison and L. V. Malthan. *USAF Stability and Control DATCOM.* Douglas Aircraft Company, Inc., 1965.

[5] C. E. Eriksen, T. J. Osse, R. D. Light, T. Wen, T. W. Lehman, P. L. Sabin, J. W. Ballard, and A. M. Chiodi. Seaglider: A long-range autonomous underwater vehicle for oceanographic research. *IEEE Journal of Oceanic Engineering*, 26(4):424–436, October 2001.

[6] T. I. Fossen. *Guidance and Control of Ocean Vehicles.* John Wiley and Sons, 1995.

[7] J. G. Graver. *Underwater Gliders: Dynamics, Control and Design.* PhD thesis, Princeton University, May 2005.

[8] S. A. Jenkins, D. E. Humphreys, J. Sherman, J. Osse, C. Jones, N. Leonard, J. Graver, R. Bachmayer, T. Clem, P. Carroll, P. Davis, J. Berry, P. Worley, and J. Wasyl. Underwater glider system study. Technical Report 53, Scripps Institution of Oceanography, `http://repositories.cdlib.org/sio/techreport/53`, May 2003.

[9] K. Karamcheti. *Principles of Ideal-Fluid Aerodynamics.* Krieger Publishing Company, 1966.

[10] H. Lamb. *Hydrodynamics.* Dover, New York, NY, sixth edition, 1932.

[11] MSNBC Associated Press. Gliders scour the deep, propelled by the sea. (`http://www.msnbc.msn.com/id/3541445/`), November 2003.

[12] D. P. Raymer. *Aircraft Design: A Conceptual Approach.* American Institute of Aeronautics and Astronautics, Inc., 2006.

[13] Dr. J. Roskam. *Airplane Deisgn - Part VI.* Roskam Aviation and Engineering Corporation, Ottawa, Kansas, 1985.

[14] J. Sherman, R. E. Davis, W. B. Owens, and J. Valdes. The autonomous underwater glider.

[15] D. C. Webb, P. J. Simonetti, and C. P. Jones. Slocum: An underwater glider propelled by environmental energy. *IEEE Journal of Oceanic Engineering*, 26(4):447–452, October 2001.

[16] F. M. White. *Viscous Fluid Flow.* McGraw-Hill, Inc., 2nd edition, 1991.